SCIENTIFIC REPORTS

OPEN

Multiscale understanding of tricalcium silicate hydration reactions

Received: 12 February 2018
Accepted: 14 May 2018
Published online: 04 June 2018

Ana Cuesta[1,2], Jesus D. Zea-Garcia[2], Diana Londono-Zuluaga[2], Angeles G. De la Torre[2], Isabel Santacruz[2], Oriol Vallcorba[1], Monica Dapiaggi[3], Susana G. Sanfélix[2,4] & Miguel A. G. Aranda[1]

Tricalcium silicate, the main constituent of Portland cement, hydrates to produce crystalline calcium hydroxide and calcium-silicate-hydrates (C-S-H) nanocrystalline gel. This hydration reaction is poorly understood at the nanoscale. The understanding of atomic arrangement in nanocrystalline phases is intrinsically complicated and this challenge is exacerbated by the presence of additional crystalline phase(s). Here, we use calorimetry and synchrotron X-ray powder diffraction to quantitatively follow tricalcium silicate hydration process: i) its dissolution, ii) portlandite crystallization and iii) C-S-H gel precipitation. Chiefly, synchrotron pair distribution function (PDF) allows to identify a defective clinotobermorite, $Ca_{11}Si_9O_{28}(OH)_2{\cdot}8.5H_2O$, as the nanocrystalline component of C-S-H. Furthermore, PDF analysis also indicates that C-S-H gel contains monolayer calcium hydroxide which is stretched as recently predicted by first principles calculations. These outcomes, plus additional laboratory characterization, yielded a multiscale picture for C-S-H nanocomposite gel which explains the observed densities and Ca/Si atomic ratios at the nano- and meso- scales.

Le Châtelier[1] already established that Portland cement hydration starts by the dissolution of calcium silicate species in water from the most soluble silicate phase. This process is followed by the precipitation of complex poorly-crystalline calcium-silicate-hydrates (generically named C-S-H gel) and the crystallization of $Ca(OH)_2$, portlandite, see overall reaction (1)[2]. C-S-H gel is the main hydrated component in Portland cement pastes, and it is the main responsible for the strength and durability of the resulting mortars and concretes. Alite, an impure form of tricalcium silicate Ca_3SiO_5, is the main phase present in Portland cements and it has a slightly variable composition due to element-substitutions[2]. The hydration of any alite shows, in addition to an initial fast (minor) dissolution, three main stages with time: i) induction (also known as dormant period), ii) acceleration; and iii) deceleration[3]. Similar kinetic profiles take place in various heterogeneous hydration processes, for instance mineral weathering[4] and glass alteration[5]. There are two main theories to explain this early-age hydration behaviour. The first is known as 'protective layer' and it consists in the precipitation of a C-S-H gel diffusion barrier on the surfaces of alite particles which density and adherence change with time. The second is known as 'geochemical model' and it is related to the alite dissolution mechanism evolving from etch pit formation to step retreat[6]. Despite one century of focused investigations, the underlying mechanism(s) for such time evolution is still strongly debated[7,8].

$$Ca_3SiO_5 + 5.2H_2O \rightarrow 1.2Ca(OH)_2 + (CaO)_{1.8}SiO_2(H_2O)_{4.0} \quad (1)$$

The hydration reactions of alite, (i) dissolution of crystalline alite, (ii) precipitation of C-S-H gel, and (iii) crystallization of portlandite, have been thoroughly studied by many techniques including laboratory X-ray powder diffraction[9–12], calorimetry[13–15], small-angle neutron scattering[16]; advanced electron microscopies[17,18], ^{29}Si magic-angle-spinning nuclear-magnetic-resonance[19,20], and theoretical simulations[21–23]. C-S-H gel has a nanocrystalline nature and so its understanding is very challenging[24] which includes the relationship with the solution

[1]ALBA Synchrotron, Carrer de la Llum 2-26. 08290 Cerdanyola del Vallès, Barcelona, Spain. [2]Departamento de Química Inorgánica, Cristalografía y Mineralogía. Universidad de Málaga, 29071, Málaga, Spain. [3]Department of Earth Sciences "Ardito Desio", University of Milan, Milano, Italy. [4]Faculty of Engineering, Østfold University College, N-1757, Halden, Norway. Correspondence and requests for materials should be addressed to M.A.G.A. (email: migarcia@cells.es)

where it is equilibrated[25]. There are many reviews addressing this component and we cite just the most relevant and recent ones[26–28]. An updated mechanism of growth of C-S-H gel has been very recently proposed[29]. It is also important to add that the hydration of alite is affected by the presence of other species. This has been very recently exemplified by the study of the influence of aluminates, added as $NaAlO_2$, on the hydration kinetics of alite which was studied by a multi technique approach including molecular dynamics simulations to investigate the dissolution step at the nanoscale[30].

Many studies have shown that the C-S-H gel aggregates contain poorly-crystalline interconnected nanoparticles described as globules, disks and foils[31–36] which enclose water within nanopores, known as gel pore water[26]. This gel water can evolve with time with consequences in C-S-H 'bulk' density[37]. It is worth noting that this water within the gel is different from the capillary pore water (also known as free water, FW) as it cannot be removed without altering the properties of the system[27]. Concerning the atomic arrangement within the nanocrystalline component of the C-S-H gel aggregates, several experimental and theoretical techniques have concluded that defective clinotobermorite is the best available approximation[37–40]. Crystalline tobermorite-14Å, $Ca_5Si_6O_{16}(OH)_2.7H_2O$, has a Ca/Si ratio and density of 0.83 and 2.19 gcm^{-3}, respectively. The corresponding values for crystalline tobermorite-11Å, $Ca_4Si_6O_{15}(OH)_2.5H_2O$, are 0.67 and 2.40 gcm^{-3}, respectively[41]. These previous observations are striking as they are not in straightforward agreement with two well-established key bulk measured properties: i) the Ca/Si ratio on the C-S-H aggregates ranges between 1.6–2.0; and ii) the density of nanoglobules (gel pore water excluded) range 2.5–2.6 $g{\cdot}cm^{-3}$[2,31,37]. Defective clinotobermorite could justify a Ca/Si atomic ratio close to 1.2–1.3, but not higher than that[42]. Very fine intermixing of C-S-H gel with calcium hydroxide has been proposed from electron microscopy[43,44] which it could explain an overall Ca/Si ratio ranging 1.6–2.0.

The aim of this work is to contribute to the understanding of both the formation and nanostructure of C-S-H gel. Firstly, we used synchrotron X-ray powder diffraction (and calorimetry) for *in situ* determining the dissolution of alite as well as the crystallization of portlandite and the precipitation of the gel. Secondly, we have employed synchrotron X-ray total scattering (and ^{29}Si MAS-NMR) to study the short- and medium- range atomic arrangement in the C-S-H gel nanoparticles. With this knowledge and observations from electron microscopy and previous reports, we propose a model for this complex heterogeneous system, developing a multiscale picture (see Fig. 1) for the hydration of alite in order to explain the observed mass densities and Ca/Si atomic ratios at the different scales. At the nanoscale, below 10 nm, C-S-H gel are composed of a fine intermixing of defective clinotobermorite, particle sizes ranging 3–5 nm with Ca/Si ratio close 1.2, and monolayers of $Ca(OH)_2$. These aggregates generate the gel pores. At the mesoscale, between 10 and 100 nm, neat C-S-H gel appears relatively heterogeneous with $(CaO)_{1.8}SiO_2(H_2O)_{4.0}$ overall composition but slightly variable Ca/Si atomic ratios in different volumes. This is now explained by slightly different defective clinotobermorite to $Ca(OH)_2$-monolayers local ratios. At the microscale, above 100 nm, the hydration reaction of alite is well known resulting in crystalline $Ca(OH)_2$, also named portlandite, C-S-H gel and capillary water, see Fig. 1.

Results

***In situ* calorimetric study.** The hydration reactions of tricalcium silicate were studied *in situ* by calorimetry and synchrotron X-ray powder diffraction (SXRPD). The particle size distribution (PSD) (diameter) for as-received alite was quite large, $D_{v,50} = 20.8\,\mu m$, see Supplementary Fig. 1a. Therefore, two additional samples were prepared, see methods, with $D_{v,50} = 7.4$ and $2.7\,\mu m$, Supplementary Fig. 1b,c, respectively. The values of $D_{v,10}$ and $D_{v,90}$ are also shown in Supplementary Fig. 1. The characterization of these three alites is given in the supplementary information. Heat flow calorimetry curves and cumulative heat released traces up to seven days are shown in Fig. 2a,b, respectively. Table 1 reports the key values obtained from the calorimetric study including the alite reaction degree that can be estimated as the overall heat of hydration for tricalcium silicate is known[2], 517 Jg^{-1}. This is an approximation as the impurities in alite can play a role as well as the structural defects. The four studied pastes are labelled as C_3S_21 µm_045, C_3S_21 µm_080, C_3S_7 µm_080 and C_3S_3 µm_080 to highlight their PSDs and water-to-alite mass ratios, i.e. 045 means a ratio of 0.45. C_3S_21 µm_080_qz and C_3S_21 µm_080_qz stands for samples with 10 wt% of quartz and their calorimetries were recorded for the sake of comparison with the SXRPD study where 10 wt% of quartz as internal standard was employed.

***In situ* synchrotron X-ray powder diffraction study.** SXRPD data taken in capillaries of unaltered pastes were analyzed by Rietveld methodology employing the internal standard method, in this case quartz, for amorphous quantification[45]. For this *in situ* study, the overall amorphous values encompass not only the C-S-H gel content but also the FW because the hydration reactions were not arrested. To a first approximation, the bound water (the crystallization water and the gel pore water) can be calculated according to reaction (1), as the amount of dissolved alite is known. Then, this calculated value is subtracted from the initial amount of water, in order to obtain the amount of FW for each hydration age. Finally, all the weight percentages were recalculated excluding the amount of FW in order to follow the evolution of the C-S-H gel component, which it includes the nanopore gel water and any amorphous calcium hydroxide.

Figure 3a shows the phase content evolution with time for C_3S_21 µm_080 paste from SXRPD data. It is worth noting that, at 5 hours of hydration (which was our first measurement), alite was partly dissolved, ≈4 wt%, and ≈4 wt% of C-S-H gel had precipitated. The crystallization of portlandite started later, close to 7.5 hours. At 14 hours, only 2.8 wt% of crystalline portlandite was measured. The hydration reaction progressed slowly up to 100 days of hydration as it can be shown in Fig. 3a. As an example, Supplementary Fig. 2a shows the Rietveld plot for this paste at 14 hours of hydration. Finally, the quantitative phase analysis results obtained at 100 days (2400 h) was 11.8, 22.7 and 62.1 wt% of unreacted alite, crystalline portlandite and C-S-H gel, respectively. The remaining content, 3.4 wt%, was belite, Ca_2SiO_4.

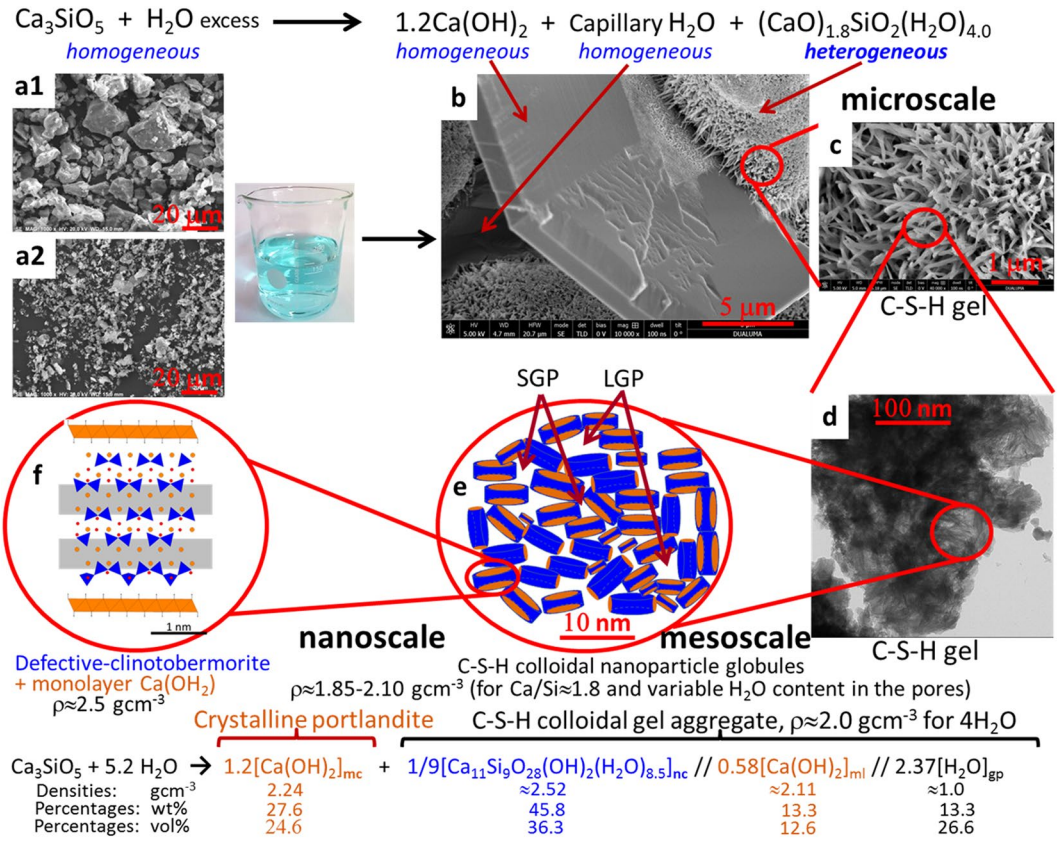

Figure 1. Schematic understanding of the alite hydration reaction at different length scales. (Top) Hydration reaction of tricalcium silicate at the microscale. (**a1**) SEM microphotograph for C_3S_21 µm. (**a2**) SEM microphotograph for C_3S_3 µm. (**b**) SEM microphotograph for C_3S_21 µm_080 paste showing a homogeneous portlandite plate microparticle, voids arising from capillary water, and three agglomerates of heterogeneous C-S-H gel. (**c**) Enlarged view of one C-S-H gel region in (**b**). (d) TEM microphotograph of C_3S_3 µm_080_ arrested:16d showing interspersed foil-like C-S-H nanoparticles at the mesoscale. (**e**) Schematic representation of the C-S-H colloidal nanoparticles of clinotobermorite (blue) and monolayer $Ca(OH)_2$ (orange) generating the small gel pores (SGP) and large gel pores (LGP) of Jennings's model (25). (**f**) Schematic representation of a single C-S-H nanoglobule composed by defective clinotobermorite and two monolayers of $Ca(OH)_2$ at the nanoscale. (Bottom) Hydration reaction of tricalcium silicate at the nanoscale highlighting the three main components of colloidal C-S-H nanocomposite: nanocrystalline clinotobermorite, amorphous (monolayer) calcium hydroxide and gel pore water. The (approximate) densities, mass and volume percentages of the different components are also given for an overall water content of four water molecules per silicate.

Figure 3b shows a similar study for C_3S_7 µm_080. For this sample, the hydration kinetics is faster. At the first measurement time, 2 hours, 4.6 wt% of alite was already dissolved, with the precipitation of ≈4 wt% of C-S-H gel and the crystallization of ≈0.4 wt% of portlandite. At 14 hours, 10.4 wt% of crystalline portlandite was measured. Supplementary Fig. 2b shows the Rietveld plot for this paste at 14 hours of hydration. A transition from the accelerated hydration reaction kinetics to decelerated kinetics is clearly observed in the phase content evolutions close to 20 hours of hydration. At 100 days of hydration, 9.3 wt% of unreacted alite was measured coexisting with 25.3 wt% of portlandite and 62.8 wt% of C-S-H gel. The remaining content, 2.6 wt% was belite, Ca_2SiO_4.

^{29}Si MAS-NMR and electron microscopy studies. The alite sample with the smallest PSD, see Supplementary Fig. 1c, was hydrated in order to minimize the amount of unreacted alite. The hydration was arrested, see methods section, in order to remove the FW, and this paste is labelled hereafter C_3S_3 µm_080_ arrested:16d. Rietveld quantitative phase analysis of LXRPD after 16 days of hydration, see Supplementary Fig. 3a, gave: 1.1 wt% of unreacted alite, 20.5 wt% of crystalline portlandite, 2.5 wt% of crystalline calcium carbonate and 75.9 wt% of amorphous content (mainly but not necessarily only C-S-H gel). Supplementary Fig. 3b shows the simulated X-ray diffraction pattern for the defective clinotobermorite T3_14sc structure, average particle size ≈5 nm, which has been used in the PDF study to fit the contribution of the nanocrystalline C-S-H gel. C_3S_3 µm_080_arrested:16 d was also studied by ^{29}Si MAS-NMR, see Fig. 4, compared to related samples in Supplementary Fig. 4, and electron microscopy, see Supplementary Figs 5 and 6. ^{29}Si MAS-NMR data give direct information about the silicate chains in C-S-H gel. The signals observed at −78.7 and −84.4 ppm were attributed to the Q^1 and Q^2 Si units, respectively[46,47]. Q^1 is associated with silicate end chain units and Q^2 indicates the presence of silicate in intermediate chain positions[48,49]. The very weak signal at −72.4 ppm corresponds to

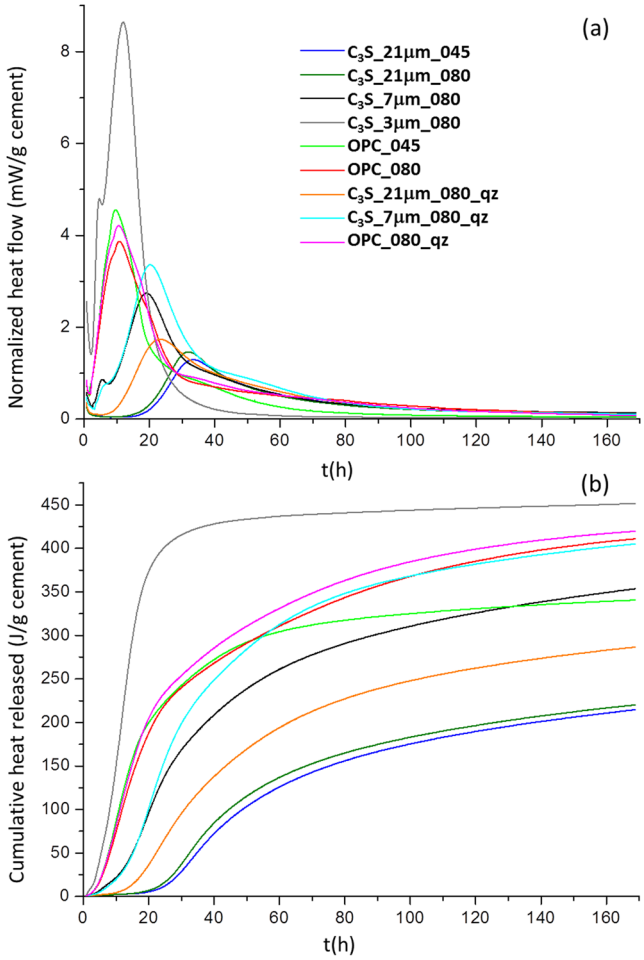

Figure 2. Calorimetric data. (**a**) Heat flow calorimetry curves and (**b**) Cumulative heat released for C3S_21 µm_045, C3S_21 µm_080, C3S_7 µm_080, C3S_3 µm_080, C3S_21 µm_080_qz, and C3S_7 µm_080_qz. Data collected in the same run for a Portland cement type-I (OPC_045 and OPC_080) and OPC_080_qz are given as reference.

Sample	BET surface area (m^2/g)	t (h)[1]	Heat-1 (J/g cement)[2]	α-1 (%)[3]	Heat-2 (J/g cement)[4]	α-2 (%)[5]
C_3S_21 µm_045	0.3(1)	33	43.2	8.4	214.2	41.4
C_3S_21 µm_080	0.3(1)	32	46.1	8.9	219.9	42.5
C_3S_21 µm_080_qz	—	23	55.4	10.7	286.3	55.4
C_3S_7 µm_080	1.1(1)	19	88.4	17.1	353.2	68.3
C_3S_7 µm_080_qz	—	20	106.1	20.5	404.9	78.3
C_3S_3 µm_080	5.2(1)	12	209.1	40.4	451.2	87.3

Table 1. Key values obtained from the alite calorimetries. [1]Time at the maximum of the heat flow curves. [2]Total heat evolved at the maximum of heat flow curves. [3]Reaction degree at the maximum of heat flow curves. [4]Total heat evolved at seven days. [5]Reaction degree at seven days.

isolated Q^0 tetrahedra from unreacted alite. The silicate MCL (mean chain length) can be determined from the expression[48], $MCL = 2(Q^1 + Q^2)/Q^1$. The deconvolution of the spectrum shown in Fig. 4 gave 70.8% for Q^1 and 24.7% for Q^2. Therefore, MCL was 2.70. This value agreed well with previous reports for early age pastes[48,49]. The ^{29}Si MAS-NMR spectra for two related samples gave very similar MCL values, see Supplementary Fig. 4. In addition, the determination of the average Ca/Si ratio is also an important parameter in any investigation of a C-S-H gel. Supplementary Fig. 5 shows a HRTEM micrograph with EDS data as an example. From 64 analysed points, the average Ca/Si atomic ratio was 1.75 ± 0.16. Supplementary Fig. 6 displays a FEGSEM micrograph (fracture cross-section).

Total-scattering pair distribution function study. The PDF data for C_3S_3 µm_080_arrested:16d, see Fig. 5, have been analyzed using the same strategy previously reported by us[40]. Initially, a high r-region, i.e.

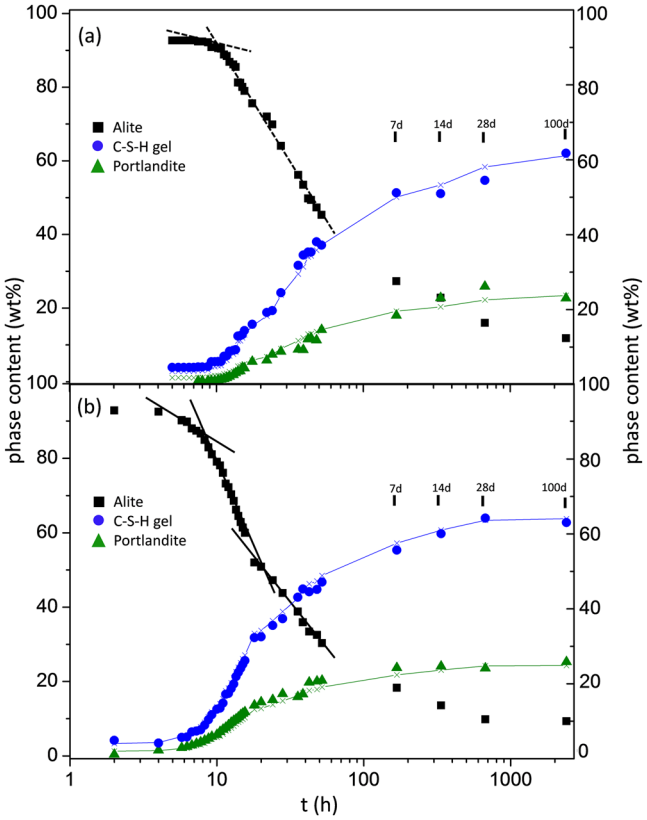

Figure 3. Quantitative phase analysis results from SXRPD. (**a**) C_3S_21 µm_080 and (**b**) C_3S_7 µm_080. The lines for C-S-H gel (blue) and portlandite (green) show the theoretical amounts expected from the measured dissolution of alite according to reaction (1).

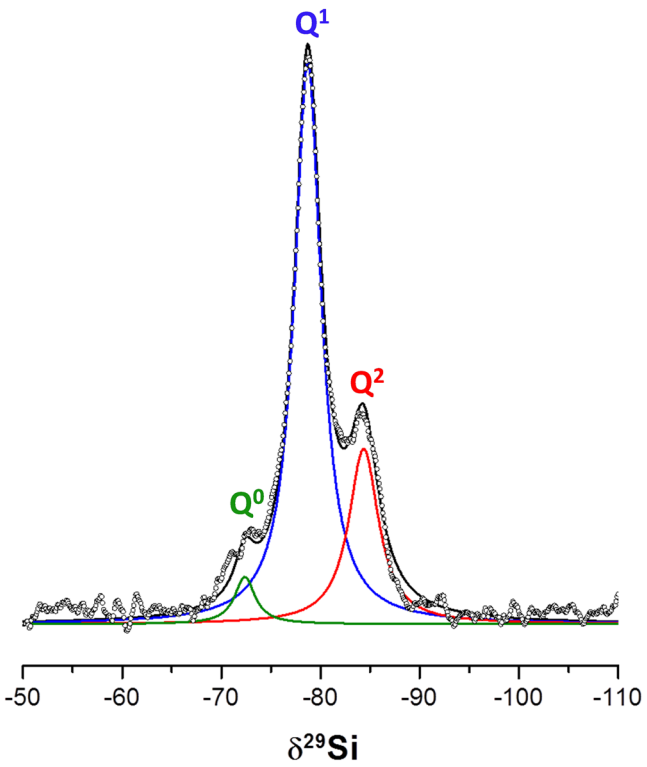

Figure 4. ^{29}Si MAS-NMR spectra for C3S_3 µm_080_arrested:16d measured. Spinning rate of 15 kHz and a magnetic field of 14.1 T.

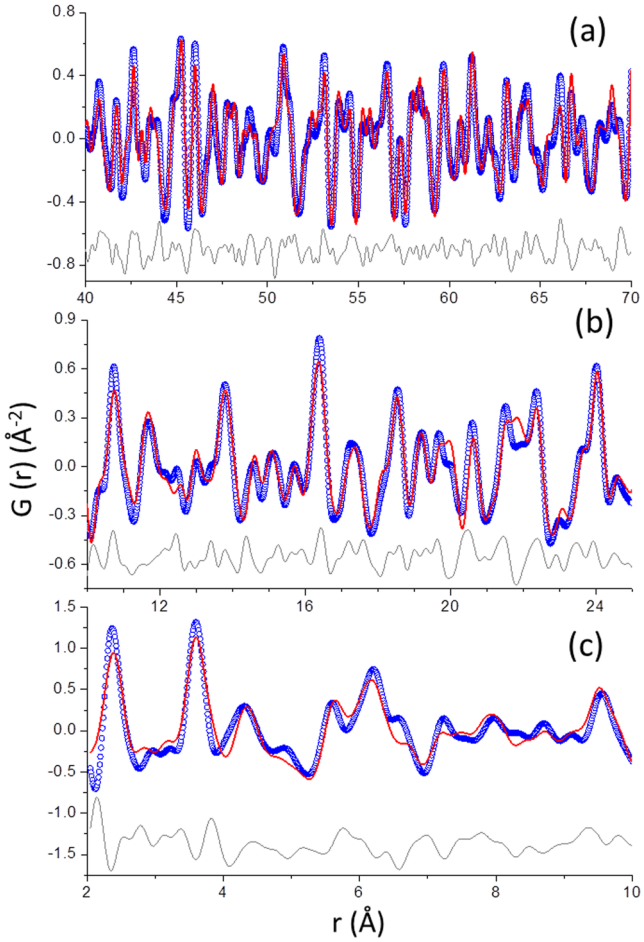

Figure 5. PDF refinements. Experimental (blue circles), fitted (red lines) and difference (grey lines) PDF patterns for C_3S_3 µm_080_arrested:16d (**a**) from 40 to 70 Å; (**b**) from 10 to 25 Å; and (**c**) from 2 to 10 Å. For details of the fits, the readers are referred to the text.

40–70 Å, was analyzed with the contributions of the crystalline phases: portlandite and alite. The low amount of alite was computed as discussed in the supplementary information. The calcite content converged to zero. After refining all parameters, the final R_W value was 26.9%. The fit is displayed in Fig. 5a. The unit cell values for portlandite converged to a = 3.595 Å and c = 4.918 Å. Secondly, all the previously determined parameters were kept fixed and the contribution from the nanocrystalline component of C-S-H gel was investigated in the r-region, from 10 to 25 Å. As it was previously reported[40], several crystal structures have been tested (Hillebrandite, Jennite, stoichiometric Tobermorite-14, stoichiometric Tobermorites-11 (monoclinic and orthorhombic), stoichiometric clinotobermorites, and selected structural descriptions from ref.[42] which had a MCL close to 3.0) to fit the contribution of the nanocrystalline C-S-H gel, see Supplementary Table 1. Jennite structure led to the worst PDF fit as evidenced by its higher R_W value, see Supplementary Fig. 7. Hillebrandite has now been included as it has been very recently reported as a good model for the nanocrystalline component of C-S-H gel[50] but it gave a poor fit to our PDF data. Supplementary Table 1 gives the R_W values for each PDF fit and the quantitative phase analysis results. The defective clinotobermorite structure, T3_14sc[42] with $Ca_{11}Si_9O_{28}(OH)_2{\cdot}8.5H_2O$ composition, has been selected as it gave the best fit to the C-S-H gel nanoparticle contribution to the PDF profile. The unit cell values for the defective clinotobermorite T3_14sc structure converged to a = 11.255 Å, b = 7.320 Å, c = 42.415 Å and β = 94.2° and the isotropic ADPs were 0.0083 and 0.0160 Å^2 for Ca, Si, respectively. The R_W was 27.7% and the final fit is displayed in Fig. 5b. For all the PDF fits, the ADP (U-thermal displacement parameter) value for O was not refined, the value was fixed to 0.070 Å^2 with correspond to that of as received Ca_3SiO_5. The PDF fit gave the following quantitative phase analysis results: 2.2 wt% of anhydrous alite, 33.5 wt% of portlandite and 64.3 wt% of clinotobermorite.

Thirdly, the low r-region, 2 to 10 Å, was studied. The PDF fit based on the contributions of portlandite, alite and defective clinotobermorite resulted in a difference PDF curve, which was quite large, see Supplementary Fig. 8, especially in the very low r-region, suggesting an amorphous component. The scattering misfit closely corresponds to the theoretical PDF trace for an isolated monolayer of $Ca(OH)_2$ as recently suggested[39,40]. Therefore, we have included a monolayer of $Ca(OH)_2$, atoms arranged as in portlandite, in the PDF fits, see supplementary information. The fit of the difference curve indicates that this monolayer $Ca(OH)_2$ is expanded along *a* and *c* directions, 3.8 and 5.3%, respectively and compressed along *b* direction, 2.1%. Overall, the volume of

monolayer $Ca(OH)_2$ is expanded 7.0% when compared to the volume of crystalline portlandite. This volume expansion would lead to a density decrease from 2.24 gcm^{-3} in bulk portlandite to 2.11 gcm^{-3} in monolayer portlandite. The stretched monolayer portlandite structure was then used in the PDF refinement (Fig. 5c). As expected, the larger correlation in this refinement took place between the scale factors of monolayer-$Ca(OH)_2$ and crystalline-$Ca(OH)_2$, −55%. The Rw value for the final fit, without computing alite, see Fig. 5c, dropped from 57 to 38% due to the contribution of monolayer portlandite.

Discussion

The hydration kinetic of as received alite was slow with the maximum in the heat flow curve close to 30 hours, with a reaction degree of ∼9%, see Table 1 and Fig. 2. The presence of 10 wt% of crystalline quartz accelerates the hydration and the maximum takes place at 23 hours, with a reaction degree of 10.7% for the paste hydrated at a w/s = 0.80. This slow kinetics was due to the large average particle size, ≈20 μm, and its relatively high iron content, 1.1 wt% expressed as Fe_2O_3. It is known that iron[51] and chromium[52] strongly delay alite hydration. Conversely, its kinetic is only slightly dependent on the water-to-alite ratio as previously reported[14,53]. The calorimetric and SXRPD studies showed a strong acceleration of alite hydration for smaller particle size samples, see Table 1 and Figs 2 and 3, in agreement with previous reports[11,54]. It is worth noting that the small peak evident in the heat flow curve at 5 h for C_3S_7 μm_080, see Fig. 2, is very likely due to its bimodal PSD with a minimal fraction of very small particle size close to 0.6 μm, see Supplementary Fig. 1b. The acceleration due to the presence of quartz, known as 'filler effect'[55], is much more pronounced for the alite sample with the largest particles. This observation point towards that alite dissolution is kinetically the limiting reaction.

We underline that the first 45 minutes of hydration is not recorded in our calorimetric study and this could neglect the measurement of the hydration of ≈5% of alite, according to the results from the SXRPD study. In any case is worth comparing the reaction degrees from calorimetry (with quartz!), Table 1, and those obtained from the quantitative analysis of SXRPD data, Fig. 3. For C_3S_21 μm_080_qz at 23 h (the time of the maximum of the heat flow curve), a reaction degree (as defined by the transformed fraction) of 11% (it could be ≈16% taking into account the fast dissolution) is obtained from the calorimetric study and ≈19% is obtained from the synchrotron study. For C_3S_7 μm_080_qz at 20 h, a reaction degree of 21% (which it could be ≈26%) is obtained from the calorimetric study and ≈38% is obtained from the synchrotron study. We justify this disagreement due to the main differences between the two set of experiments: i) the rotation of the capillary in the diffraction study with its associated shear effect;[15] and ii) and the slightly higher temperature of the diffraction study when compared to the calorimetric study, see methods. It is key to compare results from different techniques but it is also important to understand the role of the different experimental conditions that sometimes are necessary to ensure the maximum attainable accuracy.

It has been reported from *in situ* laboratory powder diffraction data, Bragg-Brentano geometry, that the crystalline portlandite content was about one third smaller than that expected from alite dissolution according to reaction (1)[10,56]. This is not the case in our synchrotron powder diffraction study as the used methodology (rotating the capillary in transmission and merging data from three capillary positions), improves the accuracy of the analyses. Figure 3 also displays the expected amounts of portlandite and C-S-H gel from alite dissolution which were in very good agreement with the measured values. Finally, it is worth noting that at very early hydration ages, the measured crystalline portlandite contents are slightly smaller than the expected ones. We speculate that this could be due to the initial precipitation of amorphous calcium hydroxide.

At 100 days, the RQPA results for C_3S_21 μm_080 were 11.8, 22.7 and 62.1 wt% of unreacted alite, crystalline portlandite and C-S-H gel, respectively. The corresponding values for C_3S_7 μm_080 were 9.3, 25.3 and 62.8 wt%, respectively. According to equation (1), the expected amounts of portlandite and C-S-H gel were 23.4 and 61.4 wt%, and 24.4 and 63.7 wt%, for C_3S_21 μm_080 and C_3S_7 μm_080, respectively. The good agreement between the determined and expected contents, for both samples, indicates the accuracy of the methodology and the suitability of the stoichiometric coefficients in reaction (1).

The PDF analysis of the total scattering data for C_3S_3 μm_080_arrested:16d paste agrees well with our previous report[40]. Moreover, the very small amount of unreacted alite, lower than 2 wt%, yielded a PDF study with less uncertainties. The crystal structure which gave the best fit to the PDF data in the region 10 to 25 Å was invariably clinotobermorite, see Supplementary Table 1. We have selected defective clinotobermorite T3_14sc, $Ca_{11}Si_9O_{28}(OH)_2{\cdot}8.5H_2O$, because in addition to the very good fit this approximate structure represents a 'trimer' derived from a staggered-chain clinotobermorite[42]. More studies are needed to confirm if this structural description is the best option for the hydration of alite under different conditions and in Portland cements. Its average silicate chain length of 3.0 is in agreement with the MCL value, 2.7, obtained by ^{29}Si MAS-NMR. However, its Ca/Si ratio, 1.22, does not agree with the Ca/Si ratio of the C-S-H determined by electron microscopy, 1.75, which is widely reported in bibliography[2,44] and previously confirmed by reaction (1). However, these Ca/Si ratios are not obtained at the same probing length scales. The Ca/Si ratio of defective clinotobermorite measured by PDF analysis is obtained at the nanoscale, probing scale: 1–3 nm. The Ca/Si ratio measured by HAADF-STEM is obtained at the mesoscale, probing scale ≈50–100 nm. The Ca/Si ratios determined from FEGSEM and Rietveld refinement of SXRPD data are obtained at the microscale, probing scale >500 nm. The apparent disagreement in the Ca/Si ratios can be reconciliated by the hypothesis that C-S-H gel aggregates arising from the hydration of alite, is a composite formed by a fine intermixing at the nanoscale of defective clinotobermorite nanoglobules, sizes ≈4 nm, and amorphous $Ca(OH)_2$, size <2 nm, see Fig. 1.

The overall multiscale picture for the hydration of alite is shown in Fig. 1 where reaction (1) at the microscale is depicted on top and its breakdown at the nanoscale is depicted at the bottom. The densities of the different components are also reported as well as their percentages (mass and volume). The hypothesis of existence of monolayer $Ca(OH)_2$ and its fine intermixing with defective clinotobermorite is supported in three ways. I. The PDF analysis in the 2–10 Å region improves notably with the inclusion of monolayer portlandite, R_W decreases from 57

to 38%. Unfortunately, the analysis of the scales factors does not allow to obtain the weight percentage of the monolayer $Ca(OH)_2$ component. II. The determined expansion of monolayer $Ca(OH)_2$ in this study, 7.0%, is in agreement with the expansion recently predicted by first principles calculations when studying pure calcium hydroxide systems[57]. This density functional theory theoretical work reported the stability of monolayer $Ca(OH)_2$ and an expansion of the average Ca-O bond from 2.36 to 2.38 Å from crystalline portlandite to monolayer $Ca(OH)_2$. III. The PDF analysis in the 10–25 Å length scale gave crystalline portlandite and nanocrystalline clinotobermorite contents of 33.5 and 64.3 wt%, respectively (see Supplementary Table 1). Our model reported at the bottom of Fig. 1, and rescaled to take into account 2 wt% of unreacted alite, gives 36.8 and 61.1 wt%, respectively. The relative close agreement between these two sets of values can be also interpreted as an indirect support of the model.

Conclusion

The *in situ* SXRPD study has confirmed the stoichiometry of alite hydration reaction to yield portlandite and C-S-H gel with $(CaO)_{1.8}SiO_2(H_2O)_{4.0}$ average composition. Chiefly, by using high-resolution synchrotron PDF analysis, it has been found that C-S-H gel is heterogeneous at the nanoscale being composed of defective clinotobermorite, with approximate composition $Ca_{11}Si_9O_{28}(OH)_2{\cdot}8.5H_2O$, and monolayers of $Ca(OH)_2$. With these results and observations from electron microscopy and previous reports, a multiscale model for the hydration of alite is proposed (see Fig. 1) which explains the observed mass densities and Ca/Si atomic ratios at the relevant scales. At the nanoscale, below 10 nm, C-S-H gel are composed of a fine intermixing of defective clinotobermorite, particle sizes ranging 3–5 nm with Ca/Si ratio close 1.2 and $\rho \approx 2.5$ gcm^{-3}, and monolayers of $Ca(OH)_2$, $\rho \approx 2.1$ gcm^{-3}. The calcium silicate component justifies the previously reported nanoglobules density, $\rho \approx 2.6$ gcm^{-3}[31,37]. These aggregates generate the gel pores. At the mesoscale, between 10 and 100 nm, neat C-S-H gel appears with variable compositions, Si/Ca ratio and water content, centred at $(CaO)_{1.8}SiO_2(H_2O)_{4.0}$. This is explained by slightly different defective clinotobermorite to $Ca(OH)_2$-monolayers local ratios and the variable gel pore water. Uneven water content also justifies the observed C-S-H gel densities at this scale, 1.9–2.1 gcm^{-3}[26] At the microscale, above 100 nm, heterogeneous $(CaO)_{1.8}SiO_2(H_2O)_{4.0}$ gel and homogeneous portlandite are arranged enclosing volumes of water, termed capillary water. The picture reported here should be taken into account for developing theoretical models. Furthermore, synthetic C-S-H gels (with Ca/Si ratios <1.4) may have very different properties as the monolayer calcium hydroxide component could be absent. Finally, the new model explains a striking feature of the hydration of cements blended with fly ash where portlandite content is measured to decrease much less than predicted by thermodynamic modelling. Although portlandite is still present, the Ca/Si ratio in C-S-H is observed to decrease from close to 1.8 in plain pastes to close to 1.4 in fly ash blends[58]. This is now explained by the consumption of $Ca(OH)_2$ monolayer component of the C-S-H gel in the pozzolanic reaction.

Methods

Full details about the Methods can be found in the supplementary information

Sample preparation. Monoclinic tricalcium silicate, alite, was acquired from Mineral Research Processing M.R.PRO. Its chemical composition determined by XRF was: 72.3 wt% CaO, 25.5 wt% SiO_2, 1.1 wt% Fe_2O_3, 0.5 wt% MgO and 0.5 wt% Al_2O_3. For the *in situ* synchrotron X-ray powder diffraction studies, the anhydrous mixtures were mixed with 10.00 wt% of SiO_2 (99.5%, AlfaAesar) as an internal standard[45].

C_3S_21 µm_080 labels the paste produced by using as received alite with a water-to-alite mass ratio of 0.80. C_3S_7 µm_080: The as received alite was milled in a vibratory mill (Retsch, mod. MM200) and the resulting powder was mixed with a water-to-alite mass ratio of 0.80. For the PDF study, as received alite was attrition milled and hydrated at a water-to-solid mass ratio of 0.80 for 16 days at 20 °C. Finally, the hydration stoppage procedure was performed by solvent exchange with isopropanol and ether[59]. This sample was labelled C_3S_3 µm_080_arrested:16d.

For the sake of comparison in the calorimetry studies, an Ordinary Portland Cement (OPC) from Financiera y Minera S.A. has been used. The samples have been labelled as OPC_045, OPC_080 and OPC_080_qz to indicate the w/s mass ratios. Furthermore, label _qz denotes the OPC with added quartz as standard.

Particle Size Distribution (PSD). Average particle size and particle size distribution for the alite samples were measured using a laser analyzer, Mastersizer S, Malvern, UK.

BET surface area. The specific surface areas of the selected samples were measured by multi-point N_2 adsorption with a BET (ASAP 2420, Micromeritics, USA) instrument.

Calorimetry. The isothermal calorimetric study was performed in an eight channel Thermal Activity Monitor (TAM) instrument using glass ampoules. The heat flow was collected up to 7 days at 20 °C.

Thermal analysis. Differential thermal analysis (DTA) and thermogravimetric (TGA) measurement for C_3S_3 µm_080_arrested:16d was performed in a SDT-Q600 analyzer from TA instruments (New Castle, DE).

NMR study. ^{29}Si MAS-NMR (Magic Angle Spinning Nuclear Magnetic Resonance) spectrum for C_3S_3 µm_080_arrested:16d was recorded at RT on a Bruker AVIII HD 600 NMR spectrometer (field strength of 14.1 T) at 156.4 MHz. The Chemical shift was referenced to an external solution of tetramethylsilane.

Laboratory X-ray powder diffraction (LXRPD) with internal standard. LXRPD data for C_3S_3 µm_080_arrested:16d was collected on a D8 ADVANCE (Bruker AXS) diffractometer (SCAI – Universidad de Malaga) equipped with a Johansson monochromator, using strictly monochromatic Mo-Kα_1 radiation, $\lambda = 0.7093$ Å, in transmission geometry (θ/θ). Sample was mixed with 20 wt% of internal standard (α-Al_2O_3).

Synchrotron X-ray powder diffraction (SXRPD). For the phase evolution study, SXRPD patterns were collected in Debye-Scherrer (transmission) mode using the X-ray powder diffraction endstation of BL04-MSPD beamline at ALBA synchrotron (Barcelona, Spain). The total acquisition time was 6 min per dataset. For the PDF study, SXRPD data for C_3S_3 μm_080_arrested:16d were collected for 3 h at the same diffractometer. The temperature inside the experimental hutch was 28 °C.

Rietveld data analysis. Rietveld analyses were performed using the GSAS suite of programs and the EXPGUI graphic interface[60]. The non-crystalline content (amorphous and nanocrystalline) was determined by the internal standard methodology[45].

Pair Distribution Function data analysis. PDF experimental data were obtained using PDFgetX3[61] with $Q_{max} = 21$ Å^{-1}. Quantitative phase analysis was obtained by using the PDFgui software[62] and CMI-diffpy complex modeling software[63].

Electron microscopy study. High resolution transmission electron microscopy (HRTEM) measurements were carried out using a FEI Talos F200X microscope equipped with X FEG and super-X EDS (Energy Dispersive Spectroscopy) system with four silicon drift detectors (SDDs) which operates at an accelerating voltage of 200 kV. FEGSEM (Field Emission Gun Scanning Electron Microscopy) micrographs and EDS analysis were performed in a Helios Nanolab 650 Microscope (FEI Company) with a retractable CBS Backscatter detector (annular solid-state device) and X-Max 50 mm^2 detector (Oxford instruments).

Data Availability. All synchrotron X-ray powder diffraction raw data files underlying this article can be accessed on Zenodo at https://doi.org/10.5281/zenodo.1027759, and used under the Creative Commons Attribution license.

References

1. Le Chatelier, H. *Recherches Expérimentales sur la Constitution des Mortiers Hydrauliques* (Doctoral thesis, Faculté des Sciences de Paris, 1887).
2. Taylor, H. F. W. *Cement Chemistry* (Thomas Telford, London, 1997)
3. Bullard, J. W. *et al.* Mechanisms of Cement Hydration. *Cem. Concr. Res.* **41**, 1208–1223 (2011).
4. Nugent, M. A., Brantley, S. L. & Pantano, C. G. & Maurice, P. A. The influence of natural mineral coatings on feldspar weathering. *Nature* **395**, 588–591 (1998).
5. Cailleteau, C. *et al.* Insight into silicate-glass corrosion mechanisms. *Nat. Mater.* **7**, 978–983 (2008).
6. Scrivener, K. L., Juilland, P. & Monteiro, P. J. M. Advances in understanding hydration of Portland cement. *Cem. Concr. Res.* **78**, 38–56 (2015).
7. Nicoleau, L., Nonat, A. & Daval, D. Rate-limiting reaction of C_3S hydration - A reply to the discussion "A new view on the kinetics of tricalcium silicate hydration" by E. Gartner. *Cem. Concr. Res.* **104**, 118–122 (2018).
8. Gartner, E. Discussion of the paper "A new view on the kinetics of tricalcium silicate hydration," by L. Nicoleau and A. *Nonat, Cem. Concr. Res. 86 (2016) 1–11. Cem. Concr. Res.* **104**, 114–117 (2018).
9. Jansen, D., Bergold, S. T., Goetz-Neunhoeffer, F. & Neubauer, J. The hydration of alite: a time-resolved quantitative X-ray diffraction approach using the G-factor method compared with heat release. *J. Appl. Crystallogr.* **44**, 895–901 (2011).
10. Bergold, S. T., Goetz-Neunhoeffer, F. & Neubauer, J. Quantitative analysis of C-S-H in hydration alite pastes by *in-situ* XRD. *Cem. Concr. Res.* **53**, 119–126 (2013).
11. Bergold, S. T., Goetz-Neunhoeffer, F. & Neubauer, J. Mechanically activated alite: New insights into alite hydration. *Cem. Concr. Res.* **76**, 202–211 (2015).
12. Bergold, S. T., Goetz-Neunhoeffer, F. & Neubauer, J. Influence of the reactivity of the amorphous part of mechanically activated alite on its hydration kinetics. *Cem. Concr. Res.* **88**, 73–81 (2016).
13. Lerch, W. & Bogue, R. H. Heat of hydration of Portland cement pastes. *J. Res. Natl. Bur. Stand.* **12**, 645–664 (1934).
14. Thomas, J. J. A New Approach to Modeling the Nucleation and Growth Kinetics of Tricalcium Silicate Hydration. *J. Am. Ceram. Soc.* **90**, 3282–3288 (2007).
15. Juilland, P., Kumar, A., Gallucci, E. & Flatt, R. J. & Scrivener K. L. Effect of mixing on the early hydration of alite and OPC systems. *Cem. Concr. Res.* **42**, 1175–1188 (2012).
16. Thomas, J. J., Allen, A. J. & Jennings, H. M. Hydration Kinetics and Microstructure Development of Normal and $CaCl_2$-Accelerated Tricalcium Silicate Pastes. *J. Phys. Chem. C* **113**, 19836–19844 (2009).
17. Kjellsena, K. O. & Lagerblad, B. Microstructure of tricalcium silicate and Portland cement systems at middle periods of hydration-development of Hadley grains. *Cem. Concr. Res.* **37**, 13–20 (2007).
18. Wenzel, O. *et al.* Investigating the pore structure of the calcium silicate hydrate phase. *Mater. Character.* **133**, 133–137 (2017).
19. Bellmann, F., Damidot, D., Möser, B. & Skibsted, J. Improved evidence for the existence of an intermediate phase during hydration of tricalcium silicate. *Cem. Concr. Res.* **40**, 875–884 (2010).
20. Pustovgar, E. *et al.* Understanding silicate hydration from quantitative analyses of hydrating tricalcium silicates. *Nat. Comm.* **7**, 10952 (2016).
21. Abdolhosseini-Qomi, M. J. *et al.* Combinatorial molecular optimization of cement hydrates. *Nat. Comm.* **5**, 4960 (2014).
22. Ioannidou, K. *et al.* Mesoscale texture of cement hydrates. *Proc. Natl. Acad. Sci. USA* **113**, 2029–2034 (2016).
23. Ioannidou, K. *et al.* The crucial effect of early-stage gelation on the mechanical properties of cement hydrates. *Nat. Comm.* **7**, 12106 (2016).
24. Thomas, J. J., Jenning, H. M. & Allen, A. J. Relationships between composition and density of tobermorite, jennite, and nanoscale $CaO-SiO_2-H_2O$. *J. Phys. Chem. C* **114**, 7594–7601 (2010).
25. Lothenbach, B. & Nonat, A. Calcium silicate hydrates: solid and liquid phase composition. *Cem. Concr. Res.* **78**, 57–70 (2015).
26. Jennings, H. M. Refinements to colloid model of C-S-H in cement: CM-II. *Cem. Concr. Res.* **38**, 275–289 (2008).
27. Papatzani, S., Paine, K. & Calabria-Holley, J. A comprehensive review of the models on the nanostructure of calcium silicate hydrates. *Constr. Build. Mater.* **74**, 219–234 (2015).
28. Palkovic, S. D. *et al.* Roadmap across the mesoscale for durable and sustainable cement paste–A bioinspired approach. *Constr. Build. Mater.* **115**, 13–31 (2016).
29. Gartner, E., Maruyama, I. & Chen, J. A new model for the C-S-H phase formed during the hydration of Portland cements. *Cem. Concr. Res.* **97**, 95–106 (2017).
30. Pustovgar, E. *et al.* Influence of aluminates on the hydration kinetics of tricalcium silicate. *Cem. Concr. Res.* **100**, 245–262 (2017).

31. Allen, A. J., Thomas, J. J. & Jennings, H. M. Composition and density of nanoscale calcium-silicate-hydrate in cement. *Nat. Mater.* **6**, 311–316 (2007).
32. Masoero, E., Del Gado, E., Pellenq, R. J.-M., Ulm, F.-J. & Yip, S. Nanostructure and Nanomechanics of Cement: Polydisperse Colloidal Packing. *Phys. Rev. Lett.* **109**, 155503 (2012).
33. Chiang, W.-S. *et al*. Microstructural changes of globules in calcium–silicate–hydrate gels with and without additives determined by small-angle neutron and X-ray scattering. *J. Colloid. Interface Sci.* **398**, 67–73 (2013).
34. Cappelletto, E. *et al*. Comb-Shaped Polymers as Nanostructure Modifiers of Calcium Silicate Hydrate: A ^{29}Si Solid-State NMR Investigation. *J. Phys. Chem. C* **117**, 22947–22953 (2013).
35. Chiang, W.-S. *et al*. Multiscale structure of calcium- and magnesium-silicate-hydrate gels. *J. Mater. Chem. A* **2**, 12991–12998 (2014).
36. Yu, Z., Zhou, A. & Lau, D. Mesoscopic packing of disk-like building blocks in calcium silicate hydrate. *Sci. Rep.* **6**, 36967 (2016).
37. Muller, A. C. A., Scrivener, K. L., Gajewicz, A. M. & McDonald, P. J. Densification of C–S–H Measured by 1H NMR Relaxometry. *J. Phys. Chem. C* **117**, 403–412 (2013).
38. Rejmak, P., Dolado, J. S., Stott, M. J. & Ayuela, A. ^{29}Si Chemical Shift Anisotropies in Hydrated Calcium Silicates: A Computational Study. *J. Phys. Chem. C* **117**, 8374–8380 (2013).
39. Grangeon, S. *et al*. Quantitative X-ray pair distribution function analysis of nanocrystalline calcium silicate hydrates: a contribution to the understanding of cement chemistry. *J. Appl. Crystallogr.* **50**, 1–8 (2017).
40. Cuesta, A. *et al*. Synchrotron radiation pair distribution function analysis of gels in cements. *Crystals* **7**, 317 (2017).
41. Dharmawardhana, C. C., Misra, A. & Ching, W.-Y. Quantum Mechanical Metric for Internal Cohesion in Cement Crystals. *Sci. Rep.* **4**, 7332 (2014).
42. Richardson, I. G. Model structures for C-(A)-S-H(I). *Acta. Crystallogr. B* **70**, 903–923 (2014).
43. Thomas, J. J., Chen, J. J., Jennings, H. M. & Neumann, D. A. Ca−OH bonding in the C−S−H gel phase of tricalcium silicate and white Portland cement pastes measured by inelastic neutron scattering. *Chem. Mater.* **15**, 3813–3817 (2003).
44. Chen, J. J., Sorelli, L., Vandamme, M., Ulm, F. J. & Chanvillard, G. J. A coupled nanoindentation/SEM-EDS study on low water/cement ratio portland cement paste: evidence for C–S–H/Ca(OH)2 nanocomposites. *J. Am. Ceram. Soc.* 93, (1484–1493 (2010).
45. Aranda, M. A. G., De la Torre, A. G. & León-Reina, L. Rietveld quantitative phase analysis of OPC clinkers, cements and hydration products. *Rev. Mineral. Geochem.* **74**, 169–209 (2012).
46. Goñi, S. *et al*. Quantitative study of hydration of C_3S and C_2S by thermal Analysis. Evolution and composition of C–S–H gels formed. *J. Therm. Anal. Calorim.* **102**, 965–973 (2010).
47. Mendes, A., Gates, W. P., Sanjayan, J. G. & Collins, F. NMR, XRD, IR and synchrotron NEXAFS. *Mater. Struct.* **44**, 1773–1791 (2011).
48. Richardson, I. G. The nature of C-S-H in hardened cements. *Cem. Concr. Res.* **29**, 1131–1147 (1999).
49. Sanchez-Herrero, M. J., Fernandez-Jimenez, A. & Palomo, A. Alkaline hydration of C_2S and C_3S. *J. Am. Ceram. Soc.* **99**, 604–611 (2016).
50. Bae, S. *et al*. Pair distribution function analysis of nanostructural deformation of calcium silicate hydrate under compressive stress. *J. Am. Ceram. Soc.* **101**, 408–418 (2017).
51. Stephan, D. & Wistuba, S. Crystal structure refinement and hydration behaviour of $3CaO{\cdot}SiO_2$ solid solutions with MgO, Al_2O_3 and Fe_2O_3. *J. Eur. Ceram. Soc.* **26**, 141–148 (2006).
52. Lua, L., Xianga, C., He, Y., Wang, F. & Hu, S. Early hydration of C_3S in the presence of Cd^{2+}, Pb^{2+} and Cr^{3+} and the immobilization of heavy metals in pastes. *Constr. Build. Mater.* **152**, 923–932 (2017).
53. Kirby, D. M. & Biernacki, J. J. The Effect of Water-to-Cement Ratio on the Hydration Kinetics of Tricalcium Silicate Cements: Testing the Two- Step Hydration Hypothesis. *Cem. Concr. Res.* **42**, 1147–1156 (2012).
54. Masoero, E., Thomas, J. J. & Jennings, H. M. A reaction zone hypothesis for the effects of particle size and water-to-cement ratio on the early hydration kinetics of C_3S. *J. Am. Ceram. Soc.* **97**, 967–975 (2014).
55. Berodier, E. & Scrivener, K. Understanding the Filler Effect on the Nucleation and Growth of C-S-H. *J. Am. Ceram. Soc.* **97**, 3764–3773 (2014).
56. Bergold, S. T., Goetz-Neunhoeffer, F. & Neubauer, J. Interaction of silicate and aluminate reaction in a synthetic cement system: Implications for the process of alite hydration. *Cem. Concr. Res.* **93**, 32–44 (2017).
57. Aierken, Y. *et al*. Portlandite crystal: Bulk, bilayer, and monolayer structures. *Phys. Rev. B* **91**, 245413 (2015).
58. Lothenbach, B. & Winnefeld, F. Thermodynamic modelling of cement hydration: Portland cements – blended cements – calcium sulfoaluminate cements in *Cementitious Materials - Composition, Properties, Application* (ed Pollmann, H.) 103–143 (Walter de Gruyter, Berlin, 2017).
59. García-Mate, M. Dla, Torre, A. G., León-Reina, L., Aranda, M. A. G. & Santacruz, I. Hydration studies of calcium sulfoaluminate cements blended with fly ash. *Cem. Concr. Res.* **54**, 12–20 (2013).
60. Larson, A. C. & Von Dreele, R. B. General Structure Analysis System (GSAS). *Los Alamos National Laboratory Report LAUR*, pp 86–748 (2000).
61. Juhàs, P., Davis, T., Farrow, C. L. & Billing, S. J. L. PDFgetX3: a rapid and highly automatable program for processing powder diffraction data into total scattering pair distribution functions. *J. Appl. Crystallogr.* **46**, 560–566 (2013).
62. Farrow, C. L. *et al*. PDFfit2 and PDFgui: computer programs for studying nanostructure in crystals. *J. Phys. Condens. Matter.* **19**, 335219 (2007).
63. Juhás, P., Farrow, C. L., Yang, X., Knox, K. R. & Billinge, S. J. L. Complex modeling: a strategy and software program for combining multiple information sources to solve ill posed structure and nanostructure inverse problems. *Acta. Crystallogr. A* **71**, 562–568 (2015).

Acknowledgements

This work has been supported by Spanish MINECO through BIA2014-57658-C2-2-R, which is co-funded by FEDER, BIA2014-57658-C2-1-R and I3 (IEDI-2016-0079) grants. We also thank CELLS-ALBA (Barcelona, Spain) for providing synchrotron beam time at BL04-MSPD beamline.

Author Contributions

A.C. and M.A.G.A. designed the research; A.C., D.L.Z. and J.D.Z.G. carried out the sample preparations, I.S., I.S., J.D.Z.G., A.G.D.T., D.L.Z., S.G.S. and A.C. performed the laboratory characterization; O.V., A.C., A.G.D.T. and D.L.Z. carried out the synchrotron experiments; A.C. and M.A.G.A. analyzed the synchrotron data; M.D. contributed to the PDF analysis; A.C. and M.A.G.A. wrote the paper which was revised with contributions from all authors.

Additional Information

Supplementary information accompanies this paper at https://doi.org/10.1038/s41598-018-26943-y.

Competing Interests: The authors declare no competing interests.

Supplementary information submitted to *Scientific Reports*

Multiscale understanding of the tricalcium silicate hydration reactions

Ana Cuesta[a,b], Jesus D. Zea-Garcia[b], Diana Londono-Zuluaga[b], Angeles G. De la Torre[b], Isabel Santacruz[b], Oriol Vallcorba[a], Monica Dapiaggi[c], Susana G. Sanfélix[b,d], and Miguel A.G. Aranda[a]*

[a] ALBA Synchrotron, Carrer de la Llum 2-26. 08290 Cerdanyola del Vallès, Barcelona, Spain

[b] Departamento de Química Inorgánica. Universidad de Málaga, 29071 Málaga, Spain

[c] Department of Earth Sciences "Ardito Desio", University of Milan, Milano, Italy

[d] Faculty of Engineering, Østfold University College, N-1757 Halden, Norway

* Correspondence: migarcia@cells.es or g_aranda@uma.es

This supplementary information contains:

Supplementary Figure 3. (a) LXRPD (Mo-Kα1 radiation) Rietveld plot for C_3S_3μm_080_arrested:16d. The main peaks are labelled as follow: portlandite (•), alite (▾) and added internal standard, α-Al_2O_3 (⋆), (b) Simulated XRPD pattern for the defective clinotobermorite T3_14sc structure with particle size of approximately 5nm, using the same wavelength (Mo-Kα1 radiation) and (c) Raw SXRPD pattern for the PDF study of C_3S_3μm_080_arrested:16d paste. SXRPD pattern for the empty capillary is also shown (red line).

Supplementary Figure 4. ^{29}Si MAS-NMR spectra for (a) C3S_3μm_080_arrested:16d, (b) C3S_3μm_080_non-arrested:32d (a second preparation batch for the 3 μm alite sample) and (c) C3S_13μm_080_arrested:34d. The Mean Chain Length values are depicted and the intensity of the Q_0 resonances indicates the unreacted alite fraction. Spinning rate of 15 kHz and a magnetic field of 14.1 T.

Supplementary Figure 4. High-angle annular dark-field scanning transmission electron (HAADF-STEM) micrograph for C_3S_3μm_080_arrested:16d. Three independent analyses obtained by EDS are also included as examples.

Supplementary Figure 5. Field emission gun scanning electron (FEGSEM) micrograph for C_3S_3μm_080_arrested:16d.

Supplementary Figure 6. Experimental (blue circles), fitted (red lines) and difference (grey lines) PDF patterns for C3S_3μm_080_arrested:16d from 10 to 25 Å using (a) clinotobermorite T3_14sc and (b) Jennite. The arrows highlight interatomic distance features poorly fitted by the Jennite structural description.

Supplementary Figure 7. Experimental (blue circles) and fitted (red solid line) PDF patterns for C_3S_3μm_080_arrested:16d in the 2 to 15 Å r-range with three components: crystalline

portlandite, unreacted alite and clinotobermorite. Difference curve is shown as a grey line which clearly shows the presence of an amorphous constituent. Simulated PDF curves for a monolayer (red) and a double layer (blue) calcium hydroxide, crystalline portlandite (green) and clinotobermorite T3_14sc (pink) are also included.

Supplementary Figure 8. Thermogravimetric data for C_3S_3μm_080_arrested:16d.

6. Description of every synchrotron powder diffraction raw data set deposited open access.

7. References.

1. Extended Methods section.

Sample description. Monoclinic tricalcium silicate, alite, was acquired from Mineral Research Processing M.R.PRO. Its chemical composition determined by XRF was: 72.3 wt% CaO, 25.5 wt% SiO_2, 1.1 wt% Fe_2O_3, 0.5 wt% MgO and 0.5 wt% Al_2O_3. For the *in situ* X-ray powder diffraction studies, the anhydrous mixtures were mixed with 10.00 wt% of SiO_2 (99.5%, AlfaAesar) as an internal standard[1]. Pastes were prepared by mixing alite with water by hand in a small plastic baker for 1 min with a spatula and then immediately loaded into glass capillaries of 0.5 mm of diameter with a syringe. The capillaries were sealed with grease to avoid water loss. Capillaries which were prepared to be measured at ages of 7 days or later were kept inside closed plastic containers.

C_3S_21μm_080 labels the paste produced by using as received alite with a water-to-alite mass ratio of 0.80. C_3S_7μm_080: The as received alite was milled for 140 minutes, in cycles of 10 minutes with a rest-time between cycles of 10 minutes, in a vibratory mill (Retsch, mod. MM200). The resulting powder was mixed with a water-to-alite mass ratio of 0.80.

For the PDF study, as received alite was attrition milled (in house developed at UMA) with isopropanol for 4 hours in cycles of 10 minutes with a rest-time between cycles of 10 minutes and then dried at 100ºC for 1.5 hours. Then, this alite was hydrated at a water-to-solid mass ratio of 0.80 for 16 days. The paste was poured into a hermetically closed Teflon® cylinder for 1 day. Subsequently, the cylindrical paste was taken out and stored within demineralised boiled water for

16 days at 20ºC. Then, the paste was milled to fine powder in an agate mortar. Finally, to remove the excess of water, the sample was filtrated in a Whatman system (90 mm diameter Whatman filter with a pore size of 2.5 μm on a Teflon support) and washed twice with isopropanol and finally with ether[2]. This powder was filled in a glass capillary of 0.7 mm of diameter. This sample was labelled C_3S_3 μm_080_arrested:16d.

Particle Size Distribution (PSD). Average particle size and particle size distribution for the alite samples were measured using a laser analyzer, Mastersizer S, Malvern, UK.

Calorimetry. The isothermal calorimetric study was performed in an eight channel Thermal Activity Monitor (TAM) instrument using glass ampoules. Pastes were prepared *ex situ* by mixing for 1 min ~3 g of each sample with the appropriated water, ~2 g, and they were immediately introduced in the calorimeter. A stabilization period of 45 minutes was needed to start the measurements. The heat flow was collected up to 7 days at 20ºC.

Thermal analysis. Differential thermal analysis (DTA) and thermogravimetric (TGA) measurement for C_3S_3μm_080_arrested:16d was performed in a SDT-Q600 analyzer from TA instruments (New Castle, DE). The temperature was varied from RT to 1000°C at a heating rate of 10 °C/min. Measurements were carried out in open platinum crucibles under nitrogen flow.

NMR study. ^{29}Si MAS-NMR (Magic Angle Spinning Nuclear Magnetic Resonance) spectrum for C_3S_3μm_080_arrested:16d was recorded at RT on a Bruker AVIII HD 600 NMR spectrometer (field strength of 14.1 T) at 156.4 MHz with a 2.5 mm triple-resonance DVT probe using zirconia rotors at 15 kHz spinning rates. The experiment was performed with ^{1}H decoupling (cw sequence) by applying a single pulse ($\pi/2$), an excitation pulse of 5 μs, 30 s relaxation delay and 10800 scans. The Chemical shift was referenced to an external solution of tetramethylsilane.

Laboratory X-ray powder diffraction (LXRPD) with internal standard. LXRPD data for C_3S_3μm_080_arrested:16d was collected on a D8 ADVANCE (Bruker AXS) diffractometer (SCAI – Universidad de Malaga) equipped with a Johansson monochromator, using strictly monochromatic Mo-Kα_1 radiation, λ=0.7093 Å, in transmission geometry (θ/θ). Samples were

mixed with 20 wt% of α-Al_2O_3 (AlfaAesar 42571) as internal standard. α-Al_2O_3 was previously heated up to 1500°C for 20 hours and sieved <125 μm.

Synchrotron X-ray powder diffraction (SXRPD). For the phase evolution study, SXRPD patterns were collected in Debye-Scherrer (transmission) mode using the X-ray powder diffraction endstation of BL04-MSPD beamline at ALBA synchrotron (Barcelona, Spain)[3]. The wavelength, 0.61878(3) Å, was selected with a double-crystal Si (111) monochromator and determined by using Si640d NIST standard (a=5.43123 Å). The diffractometer is equipped with a MYTHEN detector especially suited for time-resolved and extremely good signal-to-noise ratio experiments. The glass capillaries, 0.5 mm of diameter, were rotated during data collection at a speed of 100 rpm to improve diffracting particle statistics. To improve the accuracy of the results, three SXRPD patterns were collect at three different positions of every capillary and merged to produce the final dataset. The total acquisition time was 6 min per dataset (2 minutes per pattern) over the angular range 1-35º (2θ). The temperature inside the experimental hutch was 28ºC.

For the PDF study, SXRPD data for C_3S_3μm_080_arrested:16d were collected for 3 h at the same diffractometer. The employed wavelength was 0.41236(1) Å and the glass capillary diameter was 0.7 mm. Five patterns were collected, each lasted 37 min, and merged in order to improve the signal-to-noise ratio in the large recorded angular range, 1 to 120° (2θ). No changes between individual patterns were observed.

Rietveld data analysis. Rietveld analyses were performed using the GSAS suite of programs and the EXPGUI graphic interface[4]. Final global optimized parameters were: background coefficients, zero-shift error, cell parameters, and peak shape parameters using a pseudo-Voigt function. Portlandite and alite phases presented anisotropic lineshape broadening which was fitted by using the approach based of multidimensional distribution of lattice metrics[5]. For the portlandite crystal phase preferred orientation was also optimized by employing the March−Dollase ellipsoidal preferred orientation correction algorithm[6]. The non-crystalline content (amorphous and nanocrystalline) was determined by the internal standard methodology[7,8].

Pair Distribution Function data analysis. PDF experimental data was obtained using PDFgetX3[9] with Q_{max}=21 Å^{-1}. Quantitative phase analysis information was obtained from the PDF data by using the PDFgui software[10]. Final global optimized parameters were: scale factors, unit cell parameters and ADPs parameters. The delta2 value[11,12] (low-r correlated motion peak sharpening factor) was fixed to 2 Å^2. The instrumental parameters were obtained by measuring a similar data set for crystalline nickel. Nickel PDF data analysis converged to Qdamp=0.0030 Å^{-1} and Qbroad=0.0073 Å^{-1}. The refinement of the difference curve (between 2 and 10 Å) was performed by means of CMI-diffpy complex modeling software[13], with a structural model constituted of a nanoparticle of single-portlandite, with no assumption of periodicity. Final optimized parameters were: scale factor, stretching in the three different crystallographic directions, and ADP parameter for Ca atoms. This refined nanoparticle was then used (and the structural parameters fixed), together with the crystalline phases, in the fit of the PDF (2-10 Å) again with CMI-diffpy.

Electron microscopy study. High resolution transmission electron microscopy (HRTEM) measurements were carried out using a FEI Talos F200X microscope equipped with X FEG and super-X EDS system with four silicon drift detectors (SDDs) which operates at an accelerating voltage of 200 kV. Spectra were collected in Scanning TEM (STEM) mode. The sample was placed on a 200 mesh copper grid coated with formvar and carbon. For the field emission gun scanning electron microscopy (FEGSEM) study, the selected samples (ground powder) were covered with iridium. FEGSEM micrographs and EDS analysis were performed in a Helios Nanolab 650 Microscope (FEI Company) with a retractable CBS Backscatter detector (annular solid-state device) and X-Max 50 mm^2 detector (Oxford instruments). Backscattering electron imaging (BSEI) was performed at 5 kV acceleration, and EDS analysis at 10 kV. The software AZtec (v.1.0) was used to quantify.

2. Alite sample characterization.

SXRPD data of the anhydrous as received alite, C_3S_21μm, was analyzed by Rietveld methodology employing the internal standard method for amorphous quantification. A mixture between the M_1 [14] and M_3 [15] tricalcium silicate polymorphs were needed to obtain the best fit.

The Rietveld quantitative phase analysis gave the following phase assemblage: 38.7(3) wt% of M_1-Ca_3SiO_5, 57.9(2) wt% of M_3-Ca_3SiO_5 and 3.4(2) wt% of β-Ca_2SiO_4. The amorphous content was negligible for this sample. The final unit cell parameters for the M_1-Ca_3SiO_5 converged to a=9.2990(2) Å, b=7.0847(1) Å, c=12.1984(3) Å and β=116.144(1)° and for the M_3-Ca_3SiO_5 were a=33.1289(8) Å, b=7.0561(2) Å, c=18.5844(4) Å and β=94.247(2)°.

The same analysis was performed for the vibratory milled sample, C_3S_7μm. The quantitative phase analysis results obtained were the following: 31.6(3) wt% of M_1-Ca_3SiO_5, 62.6(2) wt% of M_3-Ca_3SiO_5, 2.6(1) wt% of β-Ca_2SiO_4 and 3.2(1) wt% of amorphous content. The final unit cell parameters for the M_1-Ca_3SiO_5 were a=9.2999(2) Å, b=7.0857(2) Å, c=12.1995(3) Å and β=116.148(2)° and for the M_3-Ca_3SiO_5 were a=33.1302(9) Å, b=7.0575(3) Å, c=18.5840(5) Å and β=94.32(2)°.

The Rietveld analysis for the attrition milled sample, C_3S_3 μm, was performed by using LXRPD data. The Rietveld quantitative phase analysis was the following: 26.8(8) wt% of M_1-Ca_3SiO_5, 44.6(9) wt% of M_3-Ca_3SiO_5, 2.4(2) wt% of β-Ca_2SiO_4 and 26.3(1) wt% of amorphous content. The final unit cell parameters for the M_1-Ca_3SiO_5 converged to a=9.2900(8) Å, b=7.0714(11) Å, c=12.1878(17) Å and β=116.157(8)° and for the M_3-Ca_3SiO_5 were a=33.051(17) Å, b=7.066(2) Å, c=18.526(4) Å and β=94.42(4)°.

Finally, The PDF pattern of as received Ca_3SiO_5 was fitted with the M3 structure of Mumme [16] by using PDFGui. The obtained unit cell parameters and atomic displacement parameters (ADPs) were: a=12.213 Å, b=7.085 Å, c=9.304 Å and β=116.1°; and 0.018, 0.011 and 0.070 $Å^2$ for Ca, Si and O, respectively. These values were used for the analysis of the minor fraction present in the sample C3S_3μm_080_arrested:16d paste and only the scale factor for alite was refined.

3. Thermal analysis characterization for C_3S_3μm_080_arrested:16d.

The thermogravimetric curve for C_3S_3μm_080_arrested:16d paste is shown in Supplementary Fig. 8. Several mass loss stages are observed in thermal trace. The mass loss from RT to 250°C, 17.7 wt%, is mainly ascribed to the water release from C-S-H gel aggregates. The weight loss measured between 250°C and 400°C, 2.4 wt%, could be partly related with the dehydration of amorphous calcium hydroxide. 5.7 wt% mass loss is measured between 400°C and 550°C, centered at 455°C, which corresponds to the water loss from crystalline portlandite. Two final weight losses are evident from 550 to 1000 ºC. The one observed close to 755ºC, ≈2.0 wt%, is likely due to the CO_2 released of crystalline calcite. The other close to 660°C, ≈3.8 wt%, is very likely related to the CO_2 release from amorphous calcium carbonate and probably also to the release of organic solvent, used for the arresting of the hydration, absorbed in the C-S-H gel as previously reported[17].

The components of the gel are nanocrystalline defective clinotobermorite, amorphous (monolayer) calcium hydroxide, and water within the nanopores. The weight losses for each component can be compared with that experimentally obtained for the C3S_3μm_080_arrested:16d paste. For full reaction, the theoretical weight loss for the water gel pores, 13.27 wt%, plus the water in clinotorbemorite, 5.28 wt%, sum 18.55 wt% which is comparable with the experimental weight loss between RT to 250ºC, 17.7 wt% for this paste. Secondly, the calculated weight loss from Si-OH condensation and from amorphous $Ca(OH)_2$ is 0.62 and 3.24 wt%, respectively which can be compared with the water loss observed between 250°C and 400°C, 2.4 wt% plus 2.1 wt% from the contribution of the carbonation. Finally, the experimental water loss from crystalline portlandite, 5.7 wt% is compatible with the calculated value according to reaction (1), main text, 6.7 wt%.

4. Supplementary tables:

Supplementary Table 1. Selected results for the synchrotron PDF analysis for C_3S_3μm_080_arrested:16d paste in the 10-25 Å r-region, using different structural descriptions for the nanocrystalline fraction of C-S-H gel.

Phase	R_W (%)	Ca_3SiO_5 (wt%)	Crystalline $Ca(OH)_2$ (wt%)	Nanocrystalline fraction of C-S-H (wt%)
Hillebrandite (o), ICSD #80127	33.4	3.7	55.6	40.7
Jennite (t), ICSD #151413	33.5	3.3	46.5	50.2
Tobermorite-14 (m), ICSD #152489	33.1	2.9	44.5	52.5
Tobermorite-11 (o), ICSD #92941	28.5	2.5	38.3	59.1
Tobermorite-11 (m), ICSD #87690	28.7	2.4	36.9	60.7
Tobermorite-11 (o), ICSD #100405	28.4	2.5	37.2	60.4
Clinotobermorite (m), ICSD #90036	27.4	1.8	27.1	71.1
Clinotobermorite (t), ICSD #90034	27.9	2.0	29.8	68.3
Clinotobermorite (m), T5_14sc*	28.3	2.1	32.3	65.5
Clinotobermorite (m), T5_11sc*	28.4	1.9	28.8	69.3
Clinotobermorite (m), T3_14sc*	**27.7**	**2.2**	**33.5**	**64.3**

*Richardson, 2014 [18]; (m), (o) & (t) denotes monoclinic, orthorhombic and triclinic, respectively.

5. Supplementary Figures:

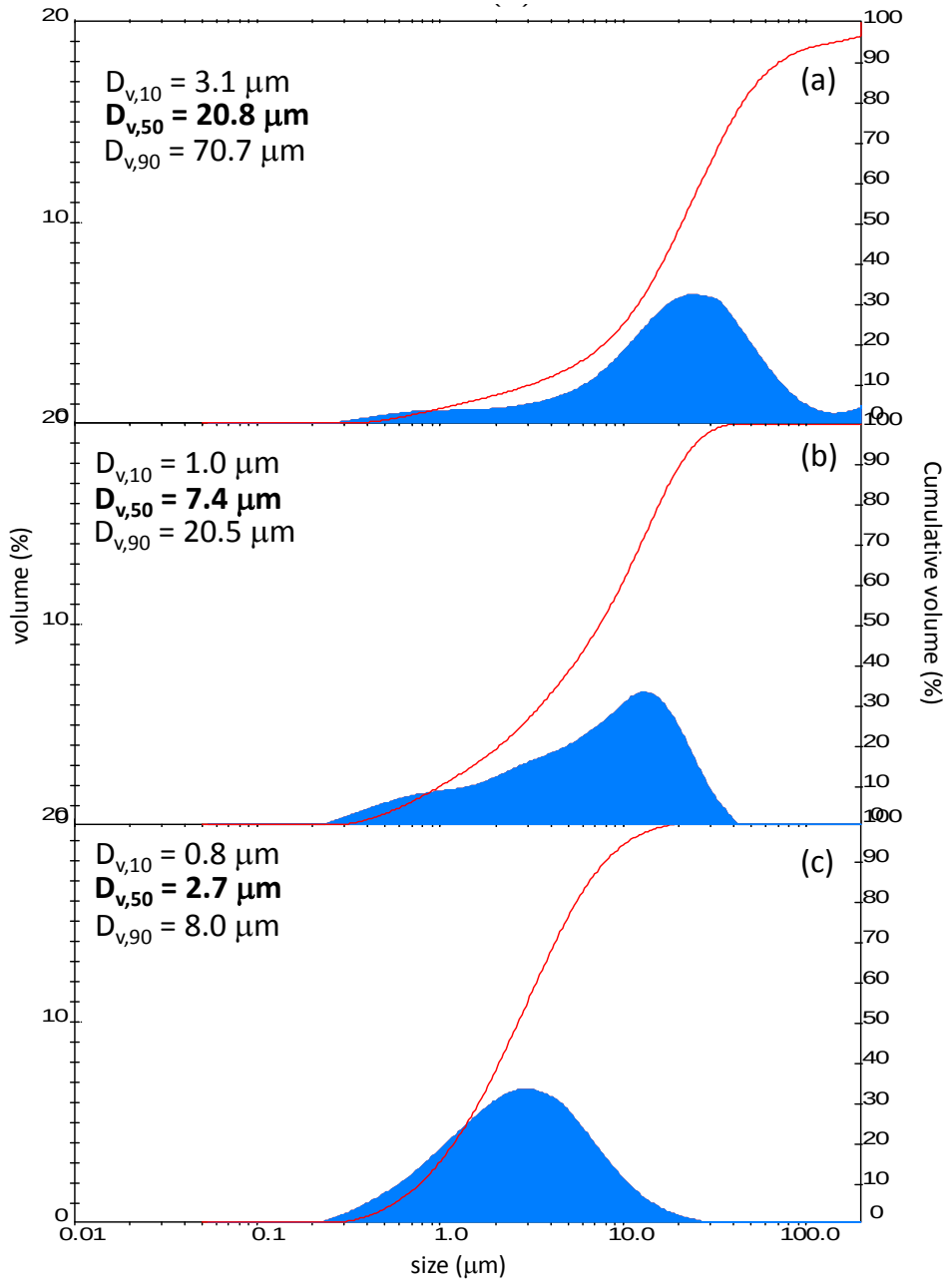

Supplementary Figure 1. Particle size distribution (diameter) and cumulative measured in volume, of the following materials (a) as received alite, (b) vibratory milled alite and (c) attrition milled alite.

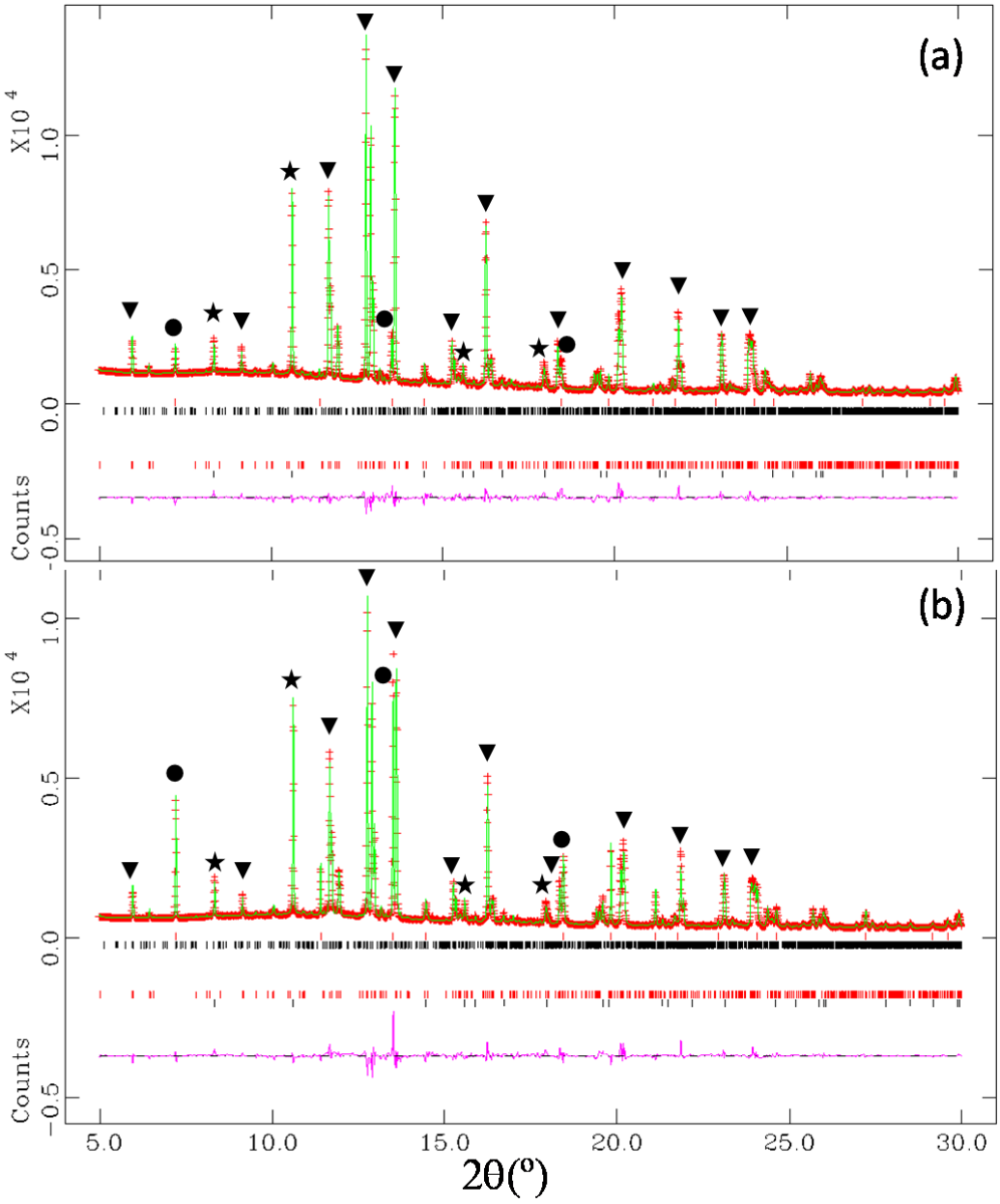

Supplementary Figure 2. SXRPD Rietveld plots at 14 hours of hydration for (a) C_3S_21µm_080 and (b) C_3S_7µm_080. The main peaks are labelled as follow: portlandite (•), alite (▾) and added internal standard, SiO_2 (⋆).

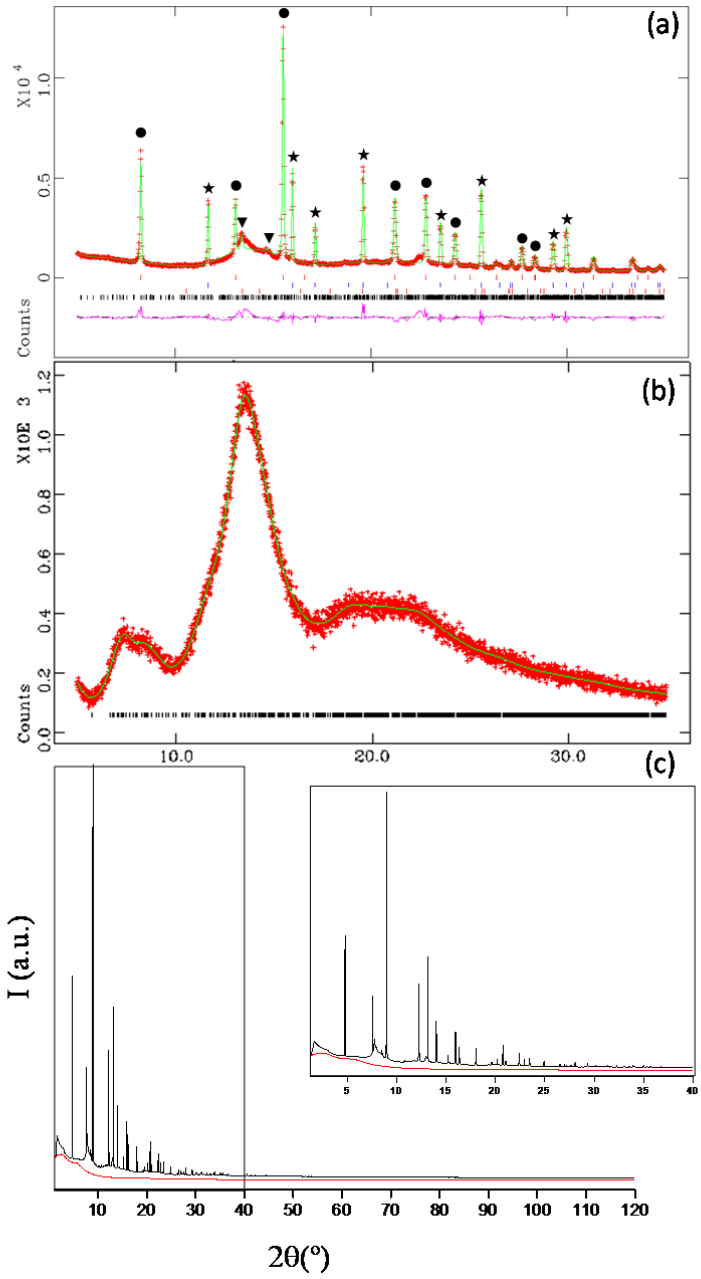

Supplementary Figure 3. (a) LXRPD (Mo-Kα1 radiation) Rietveld plot for C_3S_3µm_080_arrested:16d. The main peaks are labelled as follow: portlandite (•), alite (▾) and added internal standard, α-Al_2O_3 (⋆), (b) Simulated XRD pattern for the defective clinotobermorite T3_14sc structure with particle size of approximately 5nm, using the same wavelength (Mo-Kα1 radiation) and (c) Raw SXRPD pattern for the PDF study of C_3S_3µm_080_arrested:16d paste. SXRPD pattern for the empty capillary is also shown (red line)

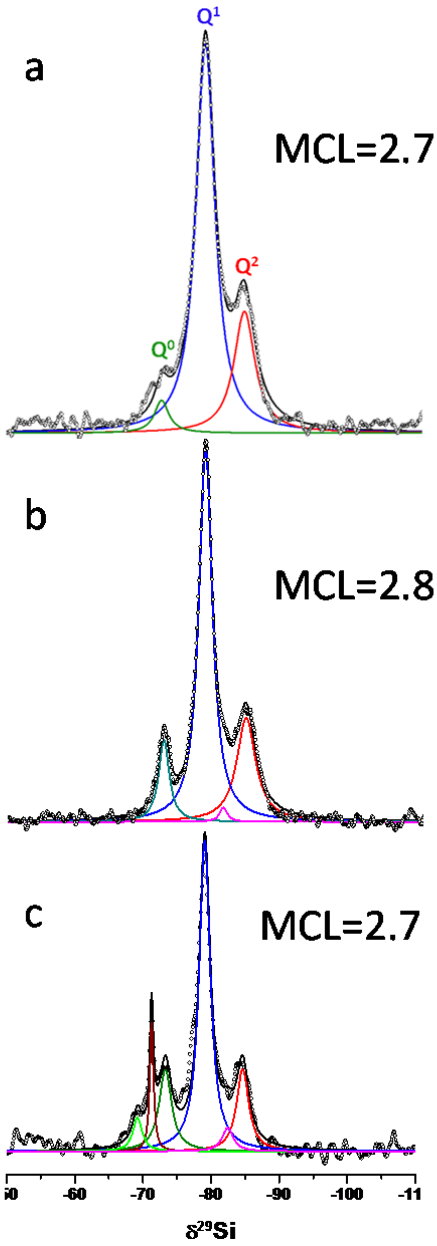

Supplementary Figure 4. ^{29}Si MAS-NMR spectra for (a) C3S_3µm_080_arrested:16d, (b) C3S_3µm_080_non-arrested:32d (a second preparation batch for the 3 µm alite sample) and (c) C3S_13µm_080_arrested:34d. The Mean Chain Length values are depicted and the intensity of the Q_0 resonances indicates the unreacted alite fraction. Spinning rate of 15 kHz and a magnetic field of 14.1 T.

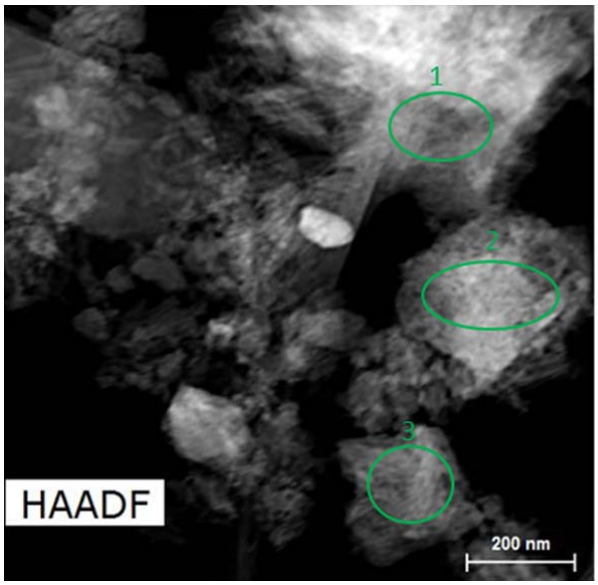

	Ca (%)	Si (%)	Ca/Si
Point 1	62.8	37.2	1.69
Point 2	64.2	35.8	1.79
Point 3	63.9	36.1	1.77

Supplementary Figure 5. High-angle annular dark-field scanning transmission electron (HAADF-STEM) micrograph for C_3S_3µm_080_arrested:16d. Three independent analyses obtained by EDS are also included as examples.

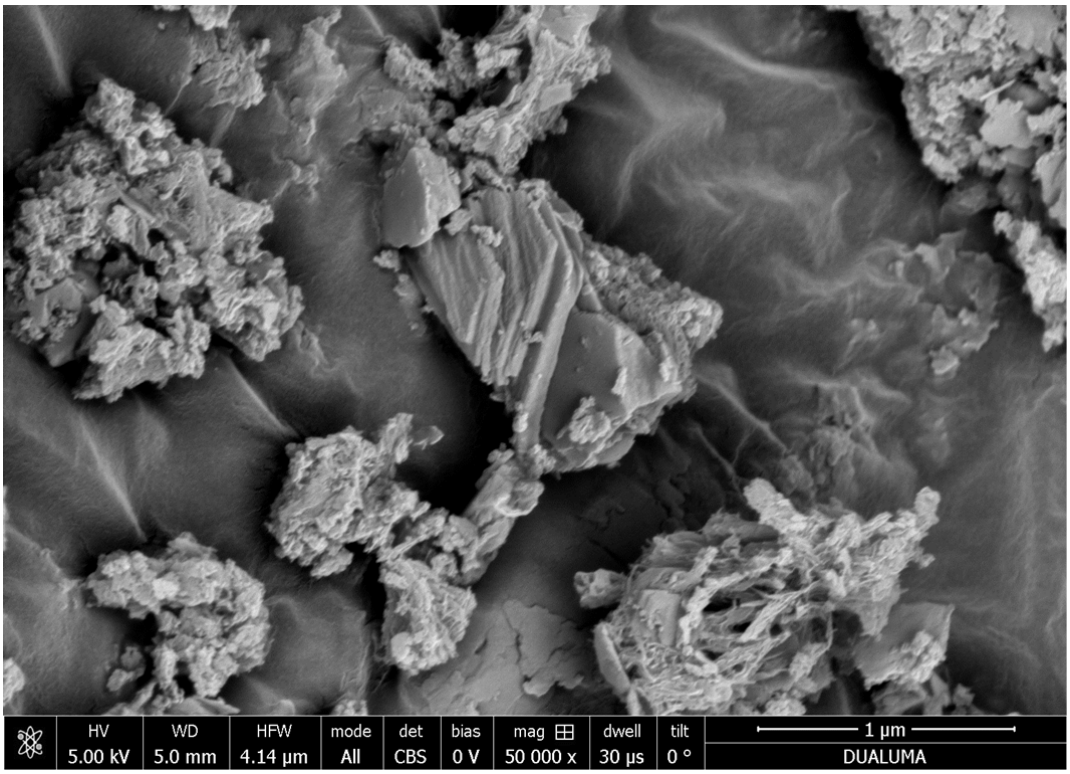

Supplementary Figure 6. Field emission gun scanning electron (FEGSEM) micrograph for C_3S_3µm_080_arrested:16d.

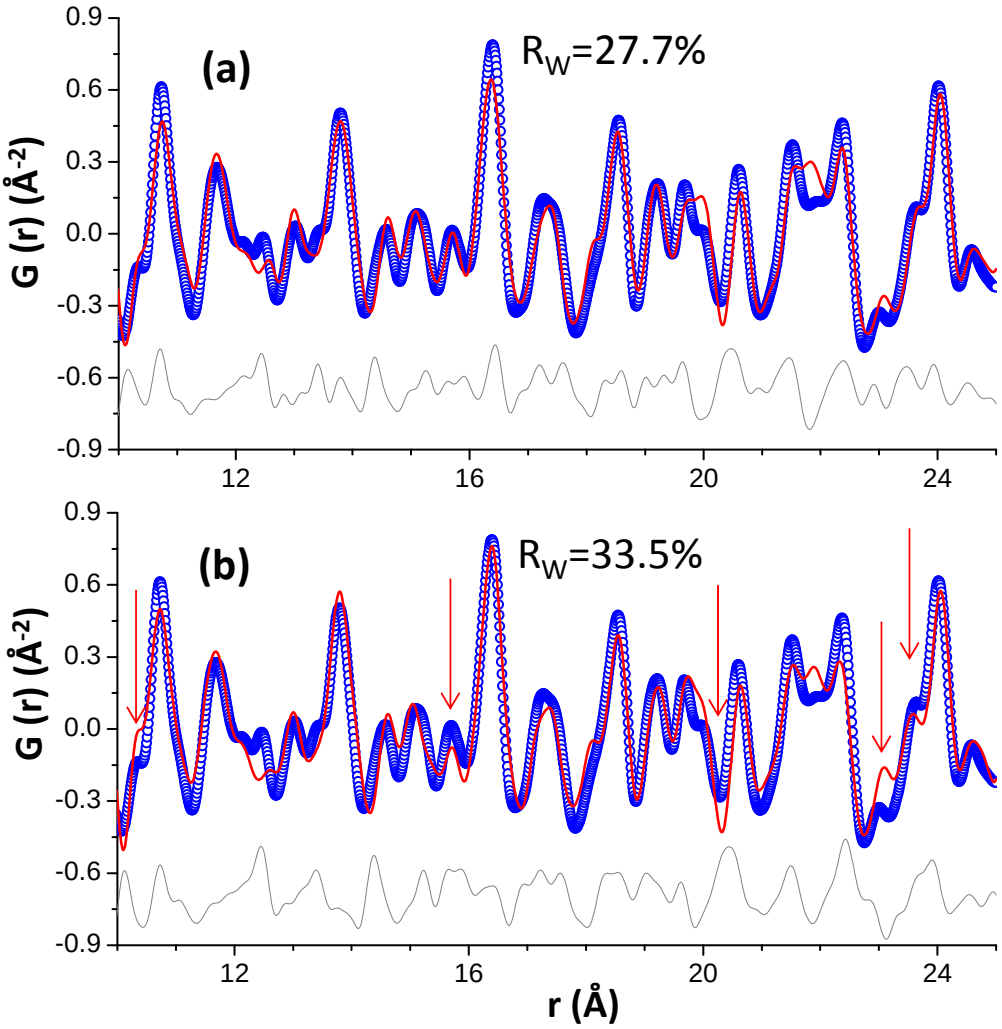

Supplementary Figure 7. Experimental (blue circles), fitted (red lines) and difference (grey lines) PDF patterns for C3S_3µm_080_arrested:16d from 10 to 25 Å using (a) clinotobermorite T3_14sc and (b) Jennite. The arrows highlight interatomic distance features poorly fitted by the Jennite structural description.

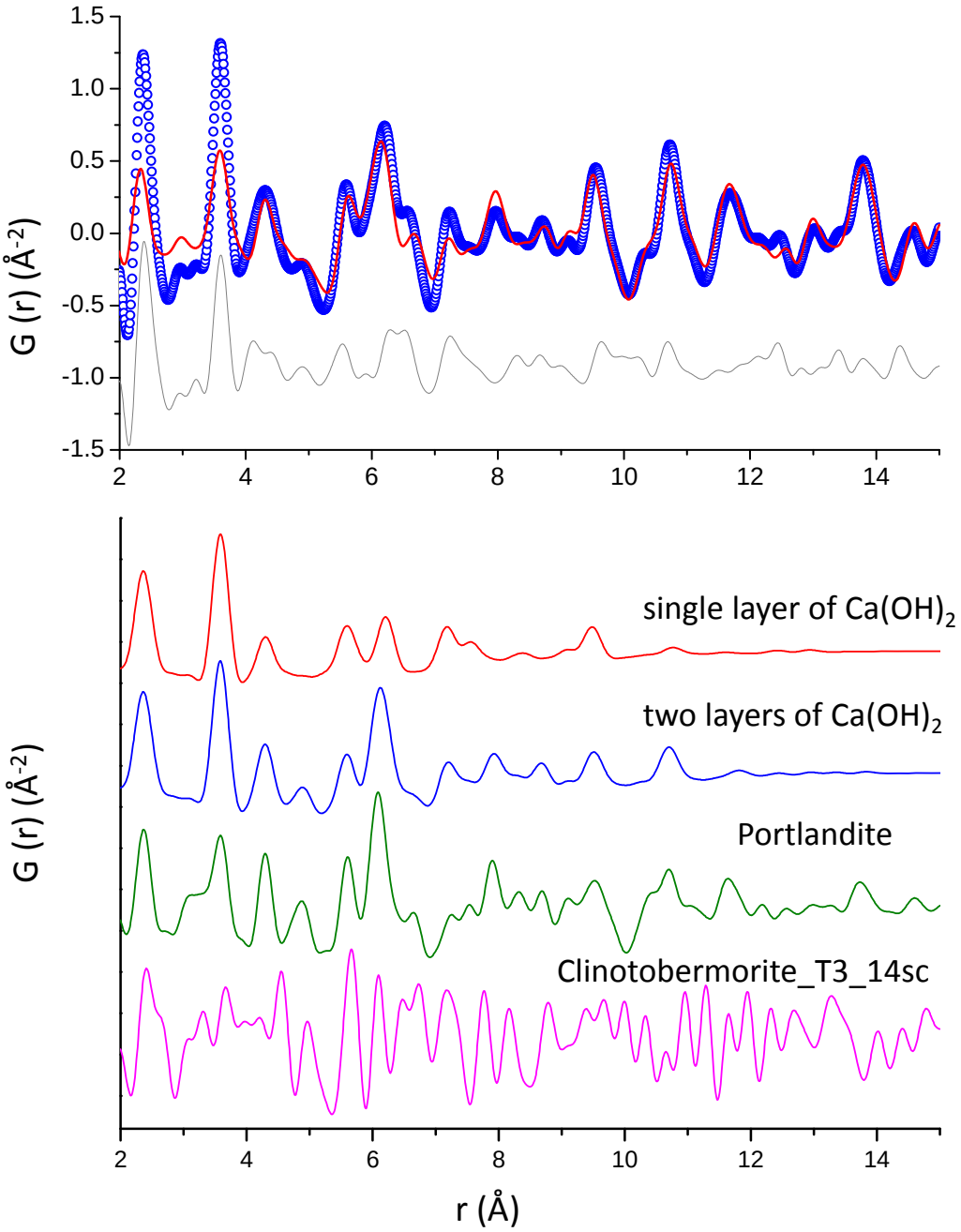

Supplementary Figure 8. Experimental (blue circles) and fitted (red solid line) PDF patterns for C_3S_3µm_080_arrested:16d in the 2 to 15 Å r-range with three components: crystalline portlandite, unreacted alite and clinotobermorite. Difference curve is shown as a grey line which clearly shows the presence of an amorphous constituent. Simulated PDF curves for a monolayer (red) and a double layer (blue) calcium hydroxide, crystalline portlandite (green) and clinotobermorite T3_14sc (pink) are also included.

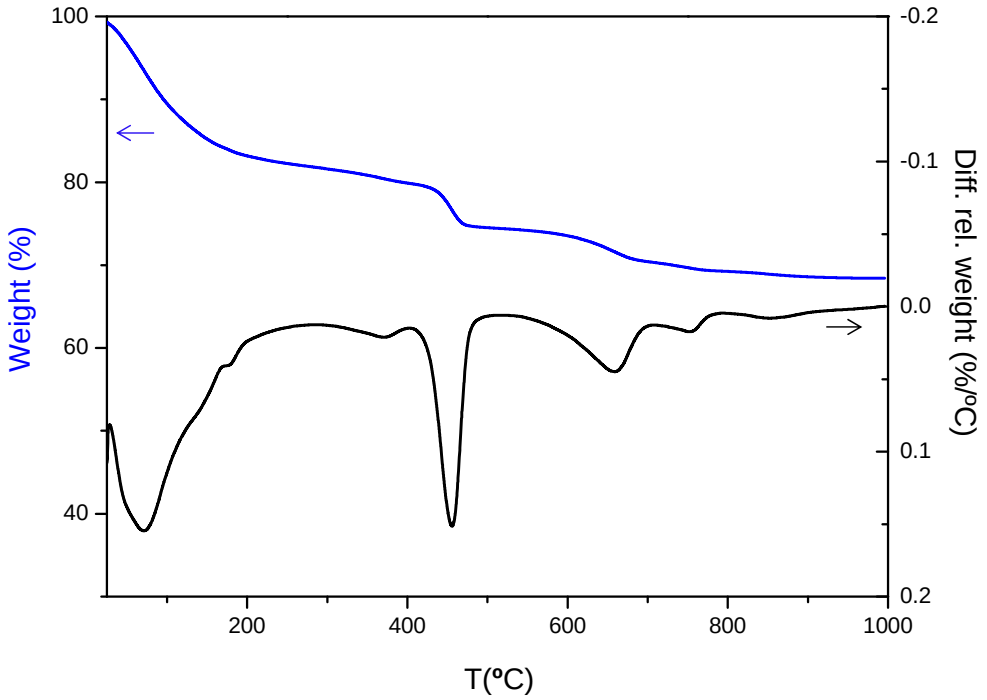

Supplementary Figure 9. Thermogravimetric data for C_3S_3µm_080_arrested:16d.

6. Description of every synchrotron powder diffraction raw data set deposited open access.

All synchrotron X-ray powder diffraction raw data files underlying this article can be accessed on Zenodo at https://doi.org/10.5281/zenodo.1027759, and used under the Creative Commons Attribution license.

Files:

Synchrotron X-ray powder diffraction study for quantitative analysis

C3S_anh_ALL.dat: anhydrous C_3S_21µm

C3S_080_cap1_5h_ALL.dat: C_3S_21µm_080 at 5h of hydration

C3S_080_cap1_ALL_01_1707132228.dat: C_3S_21µm_080 at 5.5h of hydration

C3S_080_cap1_ALL_02_1707132300.dat: C_3S_21µm_080 at 6h of hydration

C3S_080_cap1_ALL_03_1707132331.dat: C_3S_21µm_080 at 6.5h of hydration

C3S_080_cap1_ALL_04_1707140003.dat: C_3S_21µm_080 at 7h of hydration

C3S_080_cap1_ALL_05_1707140034.dat: C_3S_21µm_080 at 7.5h of hydration

C3S_080_cap1_ALL_06_1707140105.dat: C_3S_21µm_080 at 8h of hydration

C3S_080_cap1_ALL_07_1707140137.dat: C_3S_21µm_080 at 8.75h of hydration

C3S_080_cap1_ALL_08_1707140208.dat: C_3S_21µm_080 at 9.25h of hydration

C3S_080_cap1_ALL_09_1707140239.dat: C_3S_21µm_080 at 9.75h of hydration

C3S_080_cap1_ALL_10_1707140311.dat: C_3S_21µm_080 at 10.25h of hydration

C3S_080_cap1_ALL_11_1707140342.dat: C_3S_21µm_080 at 10.75h of hydration

C3S_080_cap1_ALL_12_1707140414.dat: C_3S_21µm_080 at 11.25h of hydration

C3S_080_cap1_ALL_13_1707140445.dat: C_3S_21µm_080 at 11.75h of hydration

C3S_080_cap1_ALL_14_1707140516.dat: C_3S_21µm_080 at 12.25h of hydration

C3S_080_cap1_ALL_15_1707140548.dat: C_3S_21µm_080 at 13h of hydration

C3S_080_cap1_ALL_16_1707140619.dat: C_3S_21µm_080 at 13.5h of hydration

C3S_080_cap1_ALL_17_1707140650.dat: C_3S_21µm_080 at 14h of hydration

C3S_080_cap1_ALL_18_1707140722.dat: C_3S_21µm_080 at 14.5h of hydration

C3S_080_cap1_ALL_19_1707140753.dat: C_3S_21µm_080 at 15h of hydration

C3S_080_cap1_ALL_20_1707140825.dat: C_3S_21µm_080 at 15.5h of hydration

C3S_080_cap1_17h_ALL.dat: C_3S_21µm_080 at 17.5h of hydration

C3S_080_cap1_22h_ALL.dat: C_3S_21µm_080 at 22h of hydration

C3S_080_cap1_24h_ALL.dat: C_3S_21µm_080 at 24h of hydration

C3S_080_cap1_28h_ALL.dat: C_3S_21µm_080 at 27.5h of hydration

C3S_080_cap2_36h_ALL.dat: C_3S_21µm_080 at 36h of hydration

C3S_080_cap2_39h_ALL.dat: C_3S_21µm_080 at 39h of hydration

C3S_080_cap1_42h_ALL.dat: C_3S_21µm_080 at 42h of hydration

C3S_080_cap2_44h_ALL.dat: C_3S_21µm_080 at 44h of hydration

C3S_080_cap1_48h_ALL.dat: C_3S_21µm_080 at 48h of hydration

C3S_080_cap1_52h_ALL.dat: C_3S_21µm_080 at 52h of hydration

C3S_080_7d_ALL.dat: C_3S_21µm_080 at 7d of hydration

C3S_080_14d_rep_ALL.dat: C_3S_21µm_080 at 14d of hydration

C3S_080_28d_ALL.dat: C_3S_21µm_080 at 28d of hydration

C3S_080_3m_ALL.dat: C_3S_21µm_080 at 3m of hydration

C3Sm_anh_ALL.dat: anhydrous C_3S_7µm_080

C3Sm_080_cap3_2h_ALL.dat: C_3S_7µm_080 at 2h of hydration

C3Sm_080_cap3_4h_ALL.dat: C_3S_7µm_080 at 4h of hydration

C3Sm_080_cap1_ALL_01_1707132243.dat: C_3S_7µm_080 at 5.75h of hydration

C3Sm_080_cap1_ALL_02_1707132315.dat: C_3S_7µm_080 at 6.25h of hydration

C3Sm_080_cap1_ALL_03_1707132346.dat: C_3S_7µm_080 at 6.75h of hydration

C3Sm_080_cap1_ALL_04_1707140018.dat: C_3S_7µm_080 at 7.25h of hydration

C3Sm_080_cap1_ALL_05_1707140049.dat: C_3S_7µm_080 at 7.75h of hydration

C3Sm_080_cap1_ALL_06_1707140120.dat: C_3S_7µm_080 at 8.25h of hydration

C3Sm_080_cap1_ALL_07_1707140152.dat: C_3S_7µm_080 at 8.45h of hydration

C3Sm_080_cap1_ALL_08_1707140223.dat: C_3S_7µm_080 at 9.25h of hydration

C3Sm_080_cap1_ALL_09_1707140254.dat: C_3S_7µm_080 at 10h of hydration

C3Sm_080_cap1_ALL_10_1707140326.dat: C_3S_7µm_080 at 10.5h of hydration

C3Sm_080_cap1_ALL_11_1707140357.dat: C_3S_7µm_080 at 11h of hydration

C3Sm_080_cap1_ALL_12_1707140429.dat: C_3S_7µm_080 at 11.5h of hydration

C3Sm_080_cap1_ALL_13_1707140500.dat: C_3S_7µm_080 at 12h of hydration

C3Sm_080_cap1_ALL_14_1707140531.dat: C_3S_7µm_080 at 12.5h of hydration

C3Sm_080_cap1_ALL_15_1707140603.dat: C_3S_7µm_080 at 13h of hydration

C3Sm_080_cap1_ALL_16_1707140634.dat: C_3S_7µm_080 at 13.5h of hydration

C3Sm_080_cap1_ALL_17_1707140706.dat: C_3S_7µm_080 at 14h of hydration

C3Sm_080_cap1_ALL_18_1707140737.dat: C_3S_7µm_080 at 14.5h of hydration

C3Sm_080_cap1_ALL_19_1707140808.dat: C_3S_7µm_080 at 15h of hydration

C3Sm_080_cap1_ALL_20_1707140840.dat: C_3S_7µm_080 at 15.5h of hydration

C3Sm_080_cap1_18h_ALL.dat: C_3S_7µm_080 at 18h of hydration

C3Sm_080_cap1_20h_ALL.dat: C_3S_7µm_080 at 20h of hydration

C3Sm_080_cap1_24h_ALL.dat: C_3S_7µm_080 at 24h of hydration

C3Sm_080_cap1_28h_ALL.dat: C_3S_7µm_080 at 28h of hydration

C3Sm_080_cap2_35h_ALL.dat: C_3S_7µm_080 at 35.5h of hydration

C3Sm_080_cap2_39h_ALL.dat: C_3S_7µm_080 at 38.5h of hydration

C3Sm_080_cap1_42h_ALL.dat: C_3S_7µm_080 at 42.5h of hydration

C3Sm_080_cap2_44h_ALL.dat: C_3S_7µm_080 at 44h of hydration

C3Sm_080_cap1_48h_ALL.dat: C_3S_7µm_080 at 48h of hydration

C3Sm_080_cap1_52h_ALL.dat: C_3S_7µm_080 at 52h of hydration

C3Sm_080_7d_ALL.dat: C_3S_7µm_080 at 7d of hydration

C3Sm_080_14d_ALL.dat: C_3S_7µm_080 at 14d of hydration

C3Sm_080_28d_b_ALL.dat: C_3S_7µm_080 at 28d of hydration

C3S_milled_080_3m_ALL.dat: C_3S_7µm_080 at 3m of hydration

Pair Distribution Function study for nanoscale analysis and characterization

empty0p7_ALL.dat: empty capillary.

Ni0p7_ALL.dat: Nickel sample employed as standard.

C3S_080_milled_Marzo_ALL.dat: C_3S_3µm_080_arrested:16d.

---

7. References

1. Cuesta, A. *et al.* Hydration mechanisms of two polymorphs of synthetic ye'elimite. *Cem. Concr. Res.* **63,** 127–136 (2014).

2. García-Mate, M., De la Torre, A. G., Leon-Reina, L., Aranda, M. A. G. & Santacruz, I. Hydration studies of calcium sulfoaluminate cements blended with fly ash. *Cem. Concr. Res.* **54,** 12−20 (2013).

3. Fauth, F., Peral, I., Popescu, C. & Knapp, M. The new Material Science Powder Diffraction beamline at ALBA Synchrotron. *Powder Diffr.* **28,** S360−S370 (2013).

4. Larson, A. C. & Von Dreele, R. B. *General Structure Analysis System (GSAS).* Los Alamos National Laboratory Report LAUR, pp 86−748 (2000).

5. Stephens, P.W. Phenomenological model of anisotropic peak broadening in powder diffraction. *J. Appl. Crystallogr.* **32,** 281−289 (1999).

6. Dollase, W.A. Correction of intensities for preferred orientation in powder diffractometry: application of the March model. *J. Appl. Crystallogr.* **19,** 267−272 (1986).

7. Aranda, M. A. G., De la Torre, A. G. & León-Reina, L. Rietveld quantitative phase analysis of OPC clinkers, cements and hydration products. *Rev. Mineral. Geochem.* **74,** 169−209 (2012).

8. De la Torre, A. G., Bruque, S. & Aranda, M. A. G. Rietveld quantitative amorphous content analysis. *J. Appl. Crystallogr.* **34,** 196−202 (2001).

9. Juhàs, P., Davis, T., Farrow, C.L. & Billinge, S. J. L. PDFgetX3: a rapid and highly automatable program for processing powder diffraction data into total scattering pair distribution functions. *J. Appl. Crystallogr.* **46,** 560−566 (2013).

10. Farrow, C.L. *et al.* PDFfit2 and PDFgui: computer programs for studying nanostructure in crystals. *J. Phys. Condens. Matter.* **19,** 335219 (2007).

11. Jeong, I.-K., Heffner, R.H., Graf, M.J. & Billinge, S. J. L. Lattice dynamics and correlated atomic motion from the atomic pair distribution function. *Phys. Rev. B* **67,** 104301 (2003).

12. Jeong, I.-K., Proffen, T., Mohiuddin-Jacobs, F. & Billinge, S.J.L. Measuring Correlated Atomic Motion Using X-ray Diffraction. *J. Phys. Chem. A* **103,** 921−924 (1999).

13. Juhás, P., Farrow, C.L., Yang, X., Knox, K. R. & Billing, S. J. L. Complex modeling: a strategy and software program for combining multiple information sources to solve ill posed structure and nanostructure inverse problems. *Acta Crystallogr. A* **71,** 562−568 (2015).

14. De Noirfontaine, M. N., Dunstetter, F., Courtial, M., Gasecki, G. & Signes-Frehel, M. Polymorphism of tricalcium silicate, the major compound of Portland cement clinker: 2. Modelling alite for Rietveld analysis, an industrial challenge. *Cem Concr Res* **36,** 54–64 (2006).

15. Nishi, F., Takeuchi, Y. & Maki, I. Tricalcium silicate $Ca_3O[SiO_4]$: The Monoclinic superstructure. *Z. Kristallogr.* **172,** 297−314 (1985).

16. Mumme, W.G. Crystal structure of tricalcium silicate from a Portland cement clinker and its application to quantitative XRD analysis. *N. Jb. Miner. Abh.* **4,** 145–160 (1995).

17. Zhang, J. & Scherer, W. Comparison of methods for arresting hydration of cements. *Cem. Concr. Res*. **41,** 1024−1036 (2011).

18. Richardson, I.G. Model structures for C-(A)-S-H(I). *Acta Crystallogr. B* **70,** 903−923 (2014).